Product Description Document

Effective Angular Momentum Functions From Earth System Modelling at GFZ Helmholtz Centre for Geosciences in Potsdam

Revision 2.0 (October 29, 2026)

Robert Dill, Henryk Dobslaw, Lone Stumpe



GFZ Helmholtz Centre for Geosciences
Department 1: Geodesy
Section 1.3: Earth System Modelling

The data described in this document should be cited as:

Dobslaw, H., Dill, R. (2018). Predicting Earth Orientation Changes from Global Forecasts of Atmosphere-Hydrosphere Dynamics. Adv. Space Res., 61(4), 1047–1054, doi: 10.1016/j.asr.2017.11.044.

Contents

1 Introduction **7**
1.1 Overview on Effective Angular Momentum Functions From ESMGFZ 7
1.2 History of EAM From ESMGFZ 8

2 Theory of EOP Excitation by Global Geophysical Fluids **11**
2.1 Algorithm for EAM Calculation 11
2.2 Derivation of Prefactors α_i 13
2.3 Atmosphere Dynamics 14
2.4 Ocean Dynamics 15
2.5 Terrestrial Water and Ice Mass Changes 16
2.6 Barystatic Sea-Level Variability 16
2.7 Geodynamic Processes 16
2.8 Tides in Solid Earth, Oceans, and Atmosphere 17

3 Atmospheric EAM From ESMGFZ **19**
3.1 Atmospheric Data-Sets From ECMWF 19
3.2 Reduction of Pressure to Reference Orography 19
3.3 ECMWF Model Changes Relevant for AAM 20
3.4 Static Contribution of the Atmosphere to Ocean Bottom Pressure 21
3.5 Characteristics of AAM From ESMGFZ 22

4 Dynamic Ocean EAM From ESMGFZ **25**
4.1 OGCM Configuration 25
4.2 Atmospheric Forcing Data 25
4.3 Post-Processing of Simulated Bottom Pressure 26
4.4 Post-Processing of Simulated Mass Transport Streamfunction 26
4.5 Characteristics of OAM From ESMGFZ 27

5 Terrestrial Hydrosphere EAM From ESMGFZ **29**
5.1 LISFLOOD Model Experiment 29
5.2 Atmospheric Forcing Data 29
5.3 Characteristics of HAM From ESMGFZ 29

6 Barystatic Sea-Level Equation EAM From ESMGFZ **35**
6.1 Global Mass Conservation Approach 35
6.2 Sea-Level Variations Inferred From LISFLOOD and ECMWF 35
6.3 Characteristics of SLAM From ESMGFZ 36
6.4 Comparison With GRACE-Based SLAM From GFZ 36

7 Tidal Signals in EAM From ESMGFZ **37**
7.1 Fundamentals on Atmospheric Tides 37
7.2 Oceanic Response to Atmospheric Tides 39

8 Earth Orientation Prediction With EAM Forecasts **41**
8.1 Earth Orientation Prediction Approaches 41
8.2 AAM, OAM, HAM, and SLAM Forecasts for 10 Days 42
8.3 Improved EAM Forecasting with Machine Learning 43
8.4 90 Days-Long GAM Forecasts for Routine EOP Predictions 43

References **47**

A File Format Description **55**

B Acronyms **56**

Document Changes Log

Issue	Date	Section	Description of Change
1.0	May 31st, 2018		Initial release of document.
1.1	Mar 18th, 2019	6 7.1	Full revision of SLAM description. Doodson codes added.
2.0	Oct 10st, 2026	all	New release of 2.0 document.

Chapter 1

Introduction

1.1 Overview on Effective Angular Momentum Functions From ESMGFZ

The Earth System Modelling group at Deutsches GeoForschungsZentrum (ESMGFZ) routinely provides effective angular momentum functions (EAM) describing the non-tidal geophysical excitations of Earth orientation changes due to mass redistribution in atmosphere, oceans, and the global water cycle. The data is based on re-analysis (ERA5) and operational analysis data from the European Centre for Medium-Range Weather Forecasts (ECMWF), ocean bottom pressure and vertically integrated ocean currents obtained from an experiment with the ocean model MPIOM RL07 (Jungclaus *et al.*, 2013), and terrestrial water storage and river flow velocities out of the hydrological model OS LISFLOOD (De Roo *et al.*, 2026). Both MPIOM and LISFLOOD are consistently forced with the same atmospheric ECMWF data.

The data are dimensionless effective angular momentum functions (Brzeziński, 1992) of the matter and motion terms for atmosphere, oceans, and water storage, respectively. The temporal resolution ranges from 3 hours for atmosphere and oceans to 24 hours for the terrestrial hydrosphere and sea-level terms. Tidal variations in atmosphere and oceans for 13 most relevant frequencies are fitted and removed from the data to retain the non-tidal signals only. A long-term temporal mean was subtracted from all EAM components as estimated over the time-period 2018 – 2020 that approximately matches the length of one full solar cycle.

The non-tidal EAM of ESMGFZ and their associated forecasts are routinely updated every day. Data access and further information on the product are provided via the web-page `www.esmdata.gfz.de`, see Fig. 1.1 and in a research article that should also be used for referencing EAM from ESMGFZ:

- Dill, R. et al. Benefits of refined 10-day effective angular momentum forecasts for earth rotation parameter prediction. Journal of Geodesy 99, 15 (2025). https://doi.org/10.1007/s00190-025-01941-x

The web-page also provides access to the elastic deformations of the crust due to non-tidal atmospheric, oceanic and terrestrial water storage loading (Dill & Dobslaw, 2013). The products are strongly related to the latest version RL07 of the GRACE/-FO Atmosphere and Ocean De-Aliasing Level-1B product `isdc.gfz.de/esmdata/aod1b/` (Shihora *et al.*, 2024, 2022a; Dobslaw *et al.*, 2017). The geophysical mass distributions underneath those products are identical to the ones used for



Figure 1.1: www.esmdata.gfz.de: homepage of the ESMDATA product repository for effective angular momentum functions (EAM) and elastic surface deformation (Loading).

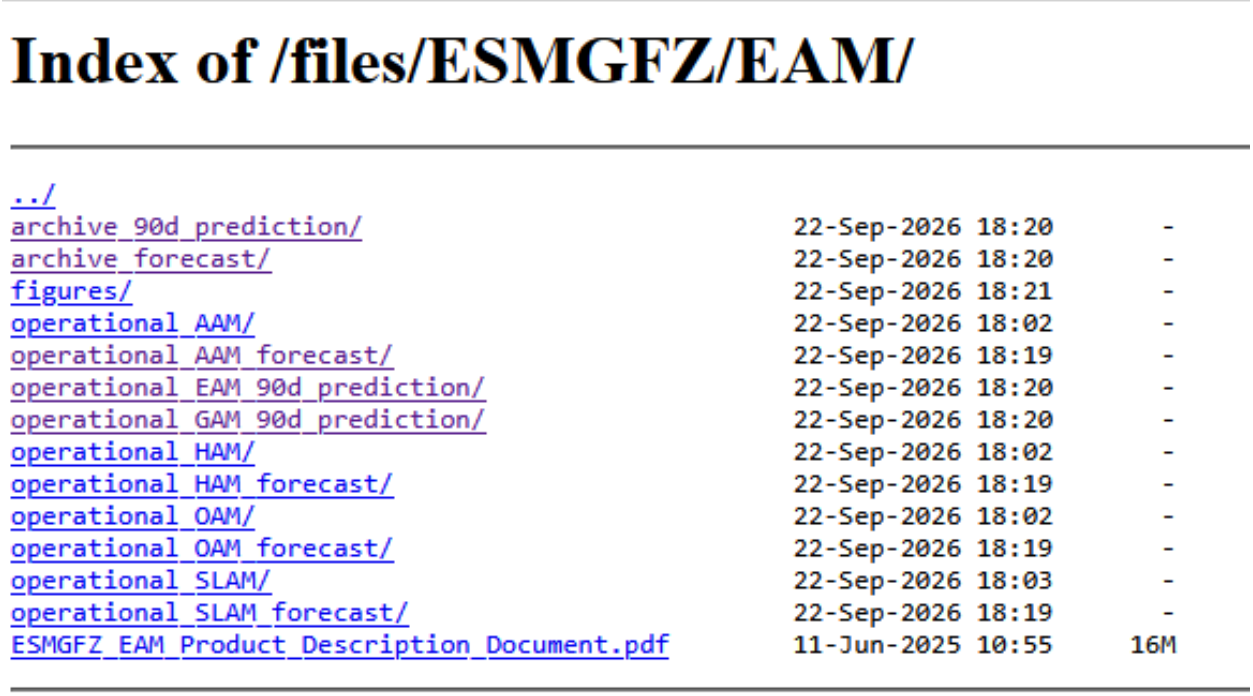
EAM calculation, and also the treatment of tides is consistent among EAM, AOD1B and the loading products. Direct file access is possible via `https://esmdata.gfz.de/files/ESMGFZ/`, see Fig. 1.2.

1.2 History of EAM From ESMGFZ

An early set of EAM is based on an ensemble of long-term simulations with the global atmospheric circulation model ECHAM3-T21 forced with observed global sea-surface temperatures and sea-ice concentrations (Stuck, 2002). The atmospheric model provides 12-hourly forcing data for the global numerical ocean model OMCT, allowing to study the impact of both the general ocean circulation and the lunisolar gravitational ocean tides on the Earth's orientation (Thomas *et al.*, 2001). The atmospheric model experiments also provide daily forcing data-sets for a land surface scheme and a hydrological discharge model to assess consequences of water mass redistribution on the continents for polar motion and ΔUT1 (Walter, 2008).

Later on, an integrated numerical model of atmosphere, oceans, and continental hydrosphere has been developed. ECOCTH is based on the atmospheric model ECHAM5-T63L31 (Roeckner *et al.*, 2003) and the MPIOM ocean general circulation model (Marsland *et al.*, 2003) with 1.5° spatial resolution. Both components are interactively coupled via the OASIS interface without additional flux corrections. A land-surface scheme for the representation of the atmosphere-land interactions is now an integral part of ECHAM5. EAM from several long-term experiments with and without the consideration of ocean tides are available (Hense *et al.*, 2009).

Atmospheric EAM have been also derived individually from the ERA-40 (1956 – 2001) and ERA-Interim (1979 – 2016) re-analyses, and from operational ECMWF analysis data (2001 – 2016). Those atmospheric data-sets are augmented by corresponding simulations with the ocean model OMCT (Dobslaw & Thomas, 2007) and the land surface and discharge model LSDM (Dill, 2008). From the year 2010 onwards, this data-set has been processed routinely for the International Earth Rotation and Reference Systems Service (IERS) in the frame of an Associated Product Center of the Global Geophysical Fluid Center (GGFC; Dobslaw *et al.*, 2010). Regular updates of this time-series ceased at the end the year 2016. In the remainder of this document, this data-set is labeled GFZ2010. The EAM series of ESMGFZ Version 1.1 was made publicly available in the



Index of /files/ESMGFZ/EAM/

../		
archive_90d_prediction/	22-Sep-2026 18:20	-
archive_forecast/	22-Sep-2026 18:20	-
figures/	22-Sep-2026 18:21	-
operational_AAM/	22-Sep-2026 18:02	-
operational_AAM_forecast/	22-Sep-2026 18:19	-
operational_EAM_90d_prediction/	22-Sep-2026 18:20	-
operational_GAM_90d_prediction/	22-Sep-2026 18:20	-
operational_HAM/	22-Sep-2026 18:02	-
operational_HAM_forecast/	22-Sep-2026 18:19	-
operational_OAM/	22-Sep-2026 18:02	-
operational_OAM_forecast/	22-Sep-2026 18:19	-
operational_SLAM/	22-Sep-2026 18:03	-
operational_SLAM_forecast/	22-Sep-2026 18:19	-
ESMGFZ_EAM_Product_Description_Document.pdf	11-Jun-2025 10:55	16M

Figure 1.2: https://esmdata.gfz.de/files/ESMGFZ/EAM/: direct file access for effective angular momentum functions (EAM).

year 2015. Version 1.2 related to the GRACE/GRACE-FO AOD1B release RL06 was published in 2017 and is labeled as GFZ2017.

EAM ESMGFZ v2.0 as described in the present document completely follows the model updates of GRACE/GRACE-FO AOD1B release RL07. Additionally, the hydrological model switched from LSDM to OS LISFLOOD and an improved OAM motion term calculation was introduced. The EAM forecast are extended from 6 days to 10 days into the future (Dill *et al.*, 2025).

Chapter 2

Theory of EOP Excitation by Global Geophysical Fluids

2.1 Algorithm for EAM Calculation

Changes in the orientation of the solid Earth are conveniently studied by applying the principle of conservation of angular momentum in the whole Earth system including the surrounding fluid layers of atmosphere, oceans, and the terrestrial hydrosphere (Gross, 2007). By summarizing the angular momentum changes from mass re-distributions in any of those sub-systems, the residual effect on the orientation of the solid Earth as represented by the terrestrial reference frame realized through a set of geodetic observatories is obtained.

The relevant inertia tensor components ΔI_{ij} are calculated from a globally gridded mass distribution at the surface of the Earth:

$$\begin{aligned}
\Delta I_{13} &= -R^2 \iint_S \cos(\phi)\sin(\phi)\cos(\theta) \quad m(\theta,\phi)\,dS \\
\Delta I_{23} &= -R^2 \iint_S \cos(\phi)\sin(\phi)\sin(\theta) \quad m(\theta,\phi)\,dS \\
\Delta I_{33} &= \;\; R^2 \iint_S \cos(\phi)^2 \qquad\qquad\quad m(\theta,\phi)\,dS,
\end{aligned} \tag{2.1}$$

with S denoting the solid angle at the Earth surface, ϕ latitude, θ longitude, R the mean radius of the Earth as given in Tab. 2.1, and $m(\theta,\phi)$ an area-normalized surface mass element which is conveniently related to pressure $p = m\,g_{\mathrm{WMO}}$ by the hydrostatic equation.

Relative angular momentum changes h_i are derived from vertically integrated zonal and meridional transports U, V via

$$\begin{aligned}
h_1 &= -R \iint_S (\,U\sin(\phi)\cos(\theta) - V\sin(\theta)\,) \quad m(\theta,\phi)\,dS \\
h_2 &= -R \iint_S (\,U\sin(\phi)\sin(\theta) + V\cos(\theta)\,) \quad m(\theta,\phi)\,dS \\
h_3 &= \;\; R \iint_S U\cos(\phi) \qquad\qquad\qquad\quad m(\theta,\phi)\,dS.
\end{aligned} \tag{2.2}$$

Table 2.1: Global geodynamic parameters employed during calculation of EAM from ESMGFZ.

parameter	value	Description
R	6371.0 km	mean radius of the Earth
G	$6.67259 \cdot 10^{-11}$ m^3 kg^{-1} s^{-2}	universal gravitational constant
g_{WMO}	9.80665 m s^{-2}	mean gravity acceleration at the Earth's surface
Ω	$7.292115 \cdot 10^{-5}$ s^{-1}	mean angular velocity of the Earth
T_{CW}	434.2 d	observed Chandler wobble period
C	$8.0365 \cdot 10^{37}$ kg m^2	$(3,3)$ component of the Earth's tensor of inertia
A	$8.0102 \cdot 10^{37}$ kg m^2	average of $(1,1)$ and $(2,2)$ components of the Earth's tensor of inertia
A_{c}	$9.1168 \cdot 10^{36}$ kg m^2	$(1,1)$ component of the Earth's tensor of inertia for the core only
ϵ_{c}	$2.546 \cdot 10^{-3}$	ellipticity of the core
$\Delta k_{\mathrm{ocn,A}}$	0.047715	oceanic equatorial rotational response
$\Delta k_{\mathrm{ocn,C}}$	0.043228	oceanic axial rotational response
k'_2	-0.305	Load Love number
$\Delta k'_{\mathrm{an}}$	-0.011	effect of mantle anelasticity on loading (real part)
n_0	0.15505	compressibility parameter (static pole tide)

Effective angular momentum functions $\chi_{i,p}$ (Brzeziński, 1992) for the mass or pressure terms are calculated from

$$\begin{aligned} \chi_{1,p} &= \frac{\alpha_1\,\alpha_2}{C-A}\Delta I_{13} \\ \chi_{2,p} &= \frac{\alpha_1\,\alpha_2}{C-A}\Delta I_{23} \\ \chi_{3,p} &= \frac{\alpha_3\,\alpha_4}{C}\Delta I_{33}. \end{aligned} \tag{2.3}$$

The corresponding motion terms for the wind or current effects $\chi_{i,w}$ read:

$$\begin{aligned} \chi_{1,w} &= \frac{\alpha_1}{\Omega\,(C-A)}h_1 \\ \chi_{2,w} &= \frac{\alpha_1}{\Omega\,(C-A)}h_2 \\ \chi_{3,w} &= \frac{\alpha_3}{\Omega\,C}h_3. \end{aligned} \tag{2.4}$$

The efficacy of mass re-distribution in the global geophysical fluid layers at the Earth surface is governed by the Earth's actual rheology. This includes in particular the elastic deformability of the Earth in response to surface loads, and also effects of a partly de-coupled rotation of the Earth's core. The prefactors α_i summarizing all those various effects are used with the following numerical values:

$$\begin{aligned} \alpha_1 &:= 1.610 \\ \alpha_2 &:= 0.684 \\ \alpha_3 &:= 1.125 \\ \alpha_4 &:= 0.750. \end{aligned} \tag{2.5}$$

The applied values differ from the ones given in Gross (2007) only for α_1. Note that we use in Eq. 2.4 the principle moments of inertia for the whole Earth. Other authors sometimes insert the mantle-only moment of inertia C_m for the axial component, thereby altering α_3 by a factor of C_m/C.

2.2 Derivation of Prefactors α_i

We are going to briefly explain now the origin of the prefactors α_i given in Eq. 2.5. The Liouville equation describing in complex notation the motion of the pole $p = p_1 + ip_2$ of an arbitrary elastically deforming elliptically layered rotating body reads as follows:

$$p + \frac{i}{\sigma}\frac{dp}{dt} = \frac{1}{C - A - D_A}\left[\left(1 + k_2' + \Delta k_{an}'\right) \cdot \Delta I + \frac{1}{\Omega} \cdot h\right], \tag{2.6}$$

with $\Delta I = \Delta I_{13} + i\Delta I_{23}$ denoting the relevant components of the tensor of inertia, and $h = h_1 + ih_2$ relative angular momentum changes. The theoretical Chandler frequency $\sigma = 2\pi/T_{\mathrm{CW}}$ is given as

$$\sigma = \frac{C - A - D_A}{A_{\mathrm{eff}} + D_A}\Omega. \tag{2.7}$$

Deviations or anomalies in the rotational period or the length of a day ΔLOD are given by

$$\Delta\mathrm{LOD} = \frac{2\pi}{\Omega} k_r \frac{1}{C_{\mathrm{eff}}}\left[\left(1 + k_{2,\mathrm{eff}}' + \Delta k_{\mathrm{an,eff}}'\right) \cdot \Delta I_{33} + \frac{1}{\Omega} \cdot h_3\right], \tag{2.8}$$

where k_r summarizes the effects of rotational deformation on the axial component as

$$k_r = \left[1 + \left(D_N + \frac{4}{3}D_C\right)\frac{1}{C_{\mathrm{eff}}}\right]^{-1} \tag{2.9}$$

The additional terms D_A, D_C, and D_n, defined as

$$\begin{aligned} D_A &= \frac{C - A}{k_s}(k_{2,\mathrm{eff}} + \Delta k_{\mathrm{ocn,A}}) \\ D_C &= \frac{C - A}{k_s}(k_{2,\mathrm{eff}} + \Delta k_{\mathrm{ocn,C}}) \\ D_n &= \frac{C - A}{k_s} n_0, \end{aligned} \tag{2.10}$$

consider changes in the inertia tensor due to the elastic response of the solid Earth on rotational changes as well as the response of the equilibrium ocean that modifies the second-degree body tide Love number k_2 by $\Delta k_{\mathrm{ocn,A}}$ and $\Delta k_{\mathrm{ocn,C}}$ for the wobble and the axial rotation, respectively. D_n considers the mean moment of inertia arising from the purely radial deformation due to the centripetal potential.

The secular Love number k_s is given by

$$k_s = \frac{3G(C - A)}{\Omega^2}\frac{1}{R^5}. \tag{2.11}$$

Elastic loading of the Earth surface for the mass terms is considered by $k_2^{'}$ including also mantle anelasticity with $k_{\mathrm{an}}^{'}$. The dynamic de-coupling between Earth's mantle and core is realized by parameters subscripted with "eff" that characterize only the effective fraction of each parameter responding to rotational or load disturbance in Earth rotation. Effective parameters are related to their unsubscripted counterparts by

$$\begin{aligned} C_{\mathrm{eff}} &= c_1 \cdot C \\ k_{2,\mathrm{eff}} &= c_2 \cdot k_2 \\ k_{2,\mathrm{eff}}^{'} &= c_3 \cdot k_2^{'} \\ A_{\mathrm{eff}} &= A - A_c \cdot (1 - c_4) \end{aligned} \tag{2.12}$$

using the coupling coefficients c_i. Assuming dynamical axisymmetry of the core-mantle boundary, we treat the mantle as fully decoupled from the core for axial changes in rotational speed leading effectively to the mantle-only parameters. According to Nam & Dickman (1990), the coupling coefficients are taken to be $1/c_1 = C/C_m = 1.129$ and $c_3 = 0.894\, C_m/C$. Therefore, c_4 equals the core's ellipticity ϵ_c since this fraction of the core inertia participates in the polar motion of the mantle. As suggested by Gross (2007), the poorly known elastic Love number $k_{2,\mathrm{eff}}$ for the rotational deformation of the mantle can be eliminated when D_A – and consequently also D_C – are derived directly from the observed Chandler period $T_{\mathrm{CW}} = 2\pi/\sigma = 434.2$ d via equation 2.7. This approach leads to $k_{2,\mathrm{eff}} = c_2 k_2 \approx 0.30978$. The assumption of a complete decoupled core for axial Earth rotation is valid for semi-diurnal to interannual periods. Note, however, that for studies concerned with decadal to millennial periods, the core and mantle would be fully coupled and our choice of coupling coefficients thus be inappropriate.

Applying those coupling coefficients c_i together with D_A, D_C, and D_n, the prefactors α_i are calculated as follows:

$$\begin{aligned} \alpha_1 &= \frac{C - A}{C - A - D_A} && \approx 1.610 \\ \alpha_2 &= 1 + k_2^{'} + \Delta k_{an}^{'} && \approx 0.684 \\ \alpha_3 &= \frac{k_r}{c_1} && \approx 1.125 \\ \alpha_4 &= 1 + c_3(k_2^{'} + \Delta k_{an}^{'}) && \approx 0.750. \end{aligned} \tag{2.13}$$

2.3 Atmosphere Dynamics

The impact of atmospheric dynamics on the time-variable rotation of the Earth has been detected already during the early years of Very Long Baseline Interferometry (VLBI) by analyzing excitation functions based on global numerical weather prediction models (Barnes *et al.*, 1983). Subsequently, the accuracy of space geodesy progressed rapidly, and also the quality of atmospheric model datasets improved due to newly available meteorological satellite observations and a break-through in data assimilation (Eubanks, 1993). Progress eventually led to the detection of signatures of the El Niño Southern Oscillation (ENSO) in seasonal variation in the length-of-day (LOD; Gross *et al.*, 1996) caused by low-frequency variations in tropospheric winds. In addition to the analysis of angular momentum estimates, atmospheric torques have been found to be beneficial for the

analysis of certain aspects of the angular momentum exchange between atmosphere and solid Earth in particular at shorter time-scales (de Viron *et al.*, 2004b).

Subsequently, numerous studies inter-compared Atmospheric Effective Angular Momentum functions (AAM) from different sources (e.g., Koot *et al.*, 2006; Masaki, 2008), and highlighted the importance of various aspects of the calculation of AAM including the accurate treatment of the surface orography (Zhou *et al.*, 2006), and the consideration of stratospheric winds in addition to tropospheric mass transports (Zhou *et al.*, 2008). The individual contributions of surface pressure variations from regional sectors to AAM where also analyzed (Nastula *et al.*, 2009), thereby opening up opportunities to principally inform atmospheric models by means of assimilating information on atmospheric angular momentum from geodetic observations (Neef & Matthes, 2012).

For the IERS, AAM estimates are disseminated by the Global Geophysical Fluid Center (GGFC) via the Special Bureau for the Atmosphere, which provides access to AAM from various sources including global re-analyes from the National Center for Environmental Prediction (NCEP), the Japan Meteorological Agency (JMA), and ECMWF.

2.4 Ocean Dynamics

Oceanic effects on Earth orientation changes were studied in more detail only during the 1990'ies when the first reliable eddy-permitting ocean general circulation models became available (Ponte & Rosen, 1993, 1994). Oceanic effects were found quickly to be of similar importance for polar motion as the contributions of the atmosphere (Dickey *et al.*, 1993; Ponte *et al.*, 1998). Even though variations of the Earth's spin rate are largely dominated by tropospheric winds, a small but relevant ocean contribution has been detected (Marcus *et al.*, 1998). OAM analysis benefited largely from the advent of ocean models with data assimilation (Ponte *et al.*, 2001), but unconstrained OGCM simulations or even models with substantially reduced physics remain important until today for the characterization of in particular high-frequency ocean mass variability at time-scales from hours to days (Bizouard & Seoane, 2010).

Early results of the Consortium for Estimating the Circulation and Climate of the Oceans (ECCO) have been analyzed extensively in terms of excitation of the Chandler wobble, the seasonal wobble (Gross *et al.*, 2003), and also decadal-scale signals as the so-called Markowitz wobble (Gross *et al.*, 2005). Other model configurations additionally considered the coupling between ocean dynamics and sea-ice (de Viron *et al.*, 2004a), between the general circulation and ocean tides (Thomas *et al.*, 2001), and other components of the climate system by means of a fully coupled global model (Zhong, 2003).The Chandler wobble analysis has been extended further by analyzing combined atmosphere-ocean excitation functions with wavelet filtering and introducing the results into a dynamic model of Earth's rotation (Seitz & Schmidt, 2005). More recent experiments explore possibilities to assimilate geodetic observations of polar motion and ΔUT1 into general ocean circulation models (Saynisch *et al.*, 2011).

Oceanic Effective Angular Momentum functions (OAM) estimates are disseminated via the Special Bureau for Oceans of IERS GGFC, which provides access to OAM from various sources including unconstrained simulations with POCM_4B (Semtner & Chervin, 1992), the global MIT OGCM (Marshall *et al.*, 1997), and in particular different development stages of the ECCO project aiming at assimilating a multitude of observational data-sets to obtain a best possible time-variable global ocean state estimate.

2.5 Terrestrial Water and Ice Mass Changes

The excitation of Earth's orientation changes by continental water storage variations largely remained unknown until the launch of the GRACE satellite mission (Tapley *et al.*, 2004) in the year 2002. Before that time, only model-based estimates existed that largely differed from each other and also from the observed polar motion (Chao & O'Connor, 1988; Chen & Wilson, 2005). Reasons for those discrepancies are plentiful and include a general lack of global observations of water mass re-distributions, and the interplay of various dynamical processes with their specific characteristics in the various climate zones. Early GRACE releases were utilized for polar motion analysis by Nastula *et al.* (2007) and Seoane *et al.* (2009). Further progress was made by using re-processed GRACE data that have a generally reduced noise level and span over more than one decade, thereby now allowing to discuss the effects of both seasonal-to-interannual variations and even secular mass changes on the path of the terrestrial pole (Adhikari & Ivins, 2016).

Hydrospheric Effective Angular Momentum functions (HAM) are available from the Special Bureau for the Hydrosphere of the IERS GGFC, which provides access to excitation estimates from hydrological models, land surface data assimilation systems, and GRACE products.

2.6 Barystatic Sea-Level Variability

Mass is continuously re-distributed among atmosphere, terrestrial storages, and the oceans. The net-inflow of water on secular time-scales causes the global sea-level to rise by currently (i.e. 2002 – 2014) more than 1 mm a^{-1} (Rietbroek *et al.*, 2016) with large interannual and in particular seasonal variations reaching amplitudes of about 1 cm (Bergmann-Wolf *et al.*, 2014) superimposed. The importance of global mass conservation for in particular seasonal LOD variations is well known for some time already (e.g., Yan & Chao, 2012). Nowadays, the corresponding excitations can be directly estimated from time-variable gravity fields of the GRACE mission. There is currently no dedicated data portal for Sea-Level Angular Momentum functions (SLAM). Its effects are sometimes included in OAM series (e.g., Dobslaw *et al.*, 2010) and thereby delivered by the Special Bureau for the Oceans; or can be derived alternatively also from GRACE mass distributions as disseminated via the Special Bureau for the Hydrosphere.

2.7 Geodynamic Processes

Various processes in the Earth's interior are expected to affect the orientation of the solid Earth. On time-scales of about 100,000 years, the Earth's upper mantle is responding viscoelastically to continental-scale glacial loads – a process commonly known as Glacial Isostatic Adjustment (GIA). A gravitationally self-consistent sea-level equation on a rotating planet was introduced by Milne & Mitrovica (1996); and a further rotational feedback on the linear momentum balance has been added to the theory by Martinec & Hagedoorn (2014). In the currently available instrumental record of Earth orientation changes, however, all GIA-related signals can be safely assumed to cause secular changes only.

The orientation of the Earth is further affected by coupling mechanisms between the core of the Earth and the surrounding lower mantle. The relevant interactions take place by means of gravitational torques caused by irregularities in the topography of the core-mantle boundary (Hinderer *et al.*, 1990), but also by electromagnetic coupling effects (Holme, 1998) not only between the mantle and the fluid outer core, but also with the solid inner core (Mound & Buffett, 2003; Dumberry, 2008). Variations in LOD at periods of about 5.9 years not explained by state-of-the-art models of

surface mass redistributions are believed to be caused by torsional Alfén waves related to occasionally observed geomagnetic jerks (Cox *et al.*, 2016). Moreover, the timing of those jerks themselves as registered in geomagnetic observatories corresponds very well with observed rapid changes in ΔUT1; provided that the Earth orientation data was low-pass filtered to suppress variations at periods shorter than 6 months and additionally corrected for the effects of near-surface geophysical fluids (Holme & de Viron, 2013).

Further episodic signals in polar motion and ΔUT1 are expected to originate from mass redistribution associated with major earthquakes. Numerical modeling of the exceptionally strong 2004 Sumatra-Andaman earthquake predicts that co-seismic deformations lead to a decrease in LOD by 0.007 ms and a shift in pole coordinates of about 2.3 mas, which still might be too small to be reliably identified in the observational record (Gross & Chao, 2006). Associated post-seismic deformations that took place after the main rupture are expected to yield even smaller signals. At the moment, there is no data portal available that provides readily applicable estimates of any of the solid Earth processes introduced above.

2.8 Tides in Solid Earth, Oceans, and Atmosphere

Tidal effects on EOP are usually treated by means of the IERS conventions (Petit & Luzum, 2010), which include both a model of the solid Earth tides and also ocean tides for a finite number of frequencies in the semi-diurnal, diurnal, and long-period bands. Possible future extensions to the conventions include an update of the sub-daily (e.g., Madzak *et al.*, 2016) and long-period (e.g., Ray & Erofeeva, 2014) ocean tide models, and the additional consideration of atmospheric tides (Schindelegger & Ray, 2014) for EOP processing, interpretation, and prediction.

Chapter 3

Atmospheric EAM From ESMGFZ

Filenames: `ESMGFZ_AAM_v2.0_03h_yyyy.asc`

3.1 Atmospheric Data-Sets From ECMWF

Atmospheric Effective Angular Momemtum functions (AAM) from ESMGFZ are based on operational and re-analysis data from the ECMWF. For 1960 – 2017, AAM is based on the fifth generation reanalysis of the European Centre for Medium-Range Weather Forecasts (ECMWF-ERA5; Hersbach *et al.*, 2020). Since 2018, AAM is based on the operational ECMWF data product. Operational NWP data-sets are available for the whole time-period as well, but their quality is drastically improving in particular in the most recent years due to increased spatial resolution, improved representation of physics in the model, and tremendous progress in data assimilation thanks to the computing resources available today.

In contrast to ERA5, the operational analysis data is typically disseminated only every 6 hours. In order to calculate AAM at a higher temporal resolution of 3 hours, we make use of short-term forecasts that are available even at hourly time-steps for the most recent years of the operational ECMWF forecasts. The combination between analysis and forecast fields is performed as suggested by Dobslaw & Thomas (2005).

3.2 Reduction of Pressure to Reference Orography

Atmospheric pressure decreases with altitude. As a rule of thumb, surface pressure at mean sea-level changes by 1 hPa – which approximately corresponds to 1 cm equivalent water height – every 8 m. Thus, atmospheric surface pressure from different numerical models need to refer to the same geopotential height before comparison or even combination into a single time-series.

For the reduction of atmospheric surface pressure to a reference orography, we make use of ECMWF's sea-level pressure diagnostic kindly made available in form of a set of FORTRAN routines, that we have adapted in order to run it independently of ECMWF's Integrated Forecast System (IFS). Within those routines, mean sea-level pressure p_{msl} is calculated as follows (Yessad, 2015):

$$p_{\mathrm{msl}} = p_s \exp\left\{\frac{\Phi_s}{R_d T_s}\left[1 - \frac{\alpha\Phi_s}{2R_d T_s} + \frac{1}{3}\left(\frac{\alpha\Phi_s}{R_d T_s}\right)^2\right]\right\}. \tag{3.1}$$

Here, p_s is atmospheric surface pressure, Φ_s is the surface geopotential, R_d is the gas constant for dry air, and T_s the surface virtual temperature extrapolated from the lowest model level nlev according to

$$T_s = T_{\mathrm{nlev}} + \alpha T_{\mathrm{nlev}} \left(\frac{p_s}{p_{\mathrm{nlev}}} - 1 \right), \tag{3.2}$$

with a temperature reduction factor α,

$$\alpha = \Gamma R_d / g_{\mathrm{WMO}}, \tag{3.3}$$

where $\Gamma = 6.5$ K/km is the standard temperature lapse rate, and $g_{\mathrm{WMO}} = 9.80665\,\mathrm{m/s^2}$ the standard gravity acceleration according to the definitions of the World Meteorological Organization (WMO). Both surface temperatures and the temperature lapse rate are slightly modified for altitudes above 2000 m and extreme surface temperatures in order to avoid extrapolation to too low pressures over high and warm surfaces, and also to too high pressures over very cold surfaces; the details are given in Yessad (2015).

In addition to reducing atmospheric surface pressure to mean sea-level, the algorithm is generally applicable to extrapolate pressure vertically to arbitrary heights. For the AAM integration, the orography of IFS version 41r1 – which was in operation at ECMWF between May 12th, 2015 and March 8th, 2016 – is chosen as a reference orography, where all surface pressure data-sets are reduced to. In case that this reference orography is locally higher than the model orography, pressure is interpolated from the nearest model levels that are obtained from integrating virtual temperatures and thus geopotential heights vertically upwards.

To demonstrate the efficacy of our approach, analysis data over 14.5 years of surface pressure out of both the operational ECMWF weather prediction model and ERA-Interim have been mapped to a common reference orography (Dobslaw *et al.*, 2016). Relative biases and residual variability between both data-sets are reduced by about one order of magnitude, thereby allowing to achieve a consistency among both data-sets at the level of about 1 hPa. Remaining differences rather reflect temperature biases and also resolution limitations of the re-analysis data-set, but are not anymore related to the local roughness in orography or to changes in the spatial resolution of the operational model. The analysis of yearly biases between operational ECMWF and ERA5 revealed best coincidence in the year 2018. Therefore, we decided to use ECMWF operational data for the AAM from January 1st, 2018 onwards, and rely on ERA5 re-analysis data for all previous years.

3.3 ECMWF Model Changes Relevant for AAM

As discussed above, operational model data from ECMWF is used to compute AAM from January 1st, 2018 onwards. At this time, cycle 45r1 was in operation, wheras at the time of publication of the AAM it was already cycle 50r1. A full documentation of changes to the operational NWP model from ECMWF is available from `www.ecmwf.int/en/forecasts/documentation-and-support/changes-ecmwf-model` and we briefly mention a subset of modifications only that are most relevant for the AAM processing.

- **January 1st, 1976**: ERA-40 is used to integrate AAM. It utilizes cycle 23r4 of the IFS with a spectral T159 spatial resolution and 60 vertical sigma layers. Analysis data is obtained from four 3D-Var assimilation windows with a length of six hours each day.

- **January 1st, 1979**: ERA-Interim is introduced that utilizes IFS cycle 31r2 with a spectral T255 model (∼79 km) with again 60 sigma levels in the vertical. A twelve-hour 4D-Var assimilation window is used in this re-analysis.
- **January 1st, 2007**: Operational ECMWF data is employed for AAM computation for the first time. Cycle 31r2 with a horizontal resolution of T799 (∼25 km) is used, the vertical resolution is 91 sigma levels. Data assimilation is still based on 12-hourly 4D-Var windows.
- **January 26th, 2010**: Cycle 36r1 increases the horizontal resolution towards T1279 (∼16 km).
- **June 25th, 2013**: Cycle 38r2 increases the vertical resolution to 137 levels, the horizontal resolution remains unchanged.
- **May 12th, 2015**: Cycle 41r1 introduces a fully revised surface orography at an otherwise unchanged horizontal and vertical resolution.
- **March 8th, 2016**: Cycle 41r2 introduces the new octhahedral horizontal grid O1280 (∼8 km). The vertical resolution remains at 137 levels.
- **June 5th, 2018**: Cycle 45r1 brings enhanced dynamic coupling between the ocean, sea ice and the atmosphere.
- **October 12th, 2021**: Cycle 47r3 improvements significantly the physical basis for moist processes leading to more accurate upper air fields, particularly tropical winds, as well as precipitation in convective regimes.
- **October 18th, 2022**: Complete new ECMWF computing facilities with ATOS in Bologna.
- **October 18th, 2022**: Cycle 49r1 increased the resolution of the ensemble of data assimilations.
- **May 12th, 2026**: Cycle 50r1 brought major changes with new ocean and sea ice models based on NEMO4-SI 3, new wave interaction with sea ice and ocean currents, and reintroduction of stratospheric humidity assimilation from radiosondes.

3.4 Static Contribution of the Atmosphere to Ocean Bottom Pressure

Ocean-bottom pressure is commonly regarded as the summed effect of the hydrostatic pressure from both the atmospheric and oceanic masses situated along the plumb line above a certain position of the sea-floor. For the representation of global bottom pressure in model data-sets, those masses are traditionally separated into an atmospheric and an oceanic contribution. The local sea-surface, however, reacts rapidly to changes in atmospheric surface pressure. As evidenced from the analysis of global sea-level variations observed with satellite altimetry, the ocean is adjusting almost perfectly to surface pressure changes at periods of a few days and longer (Wunsch & Stammer, 1997). Thus, atmospheric and oceanic contributions to ocean-bottom pressure are highly anti-correlated, and largely cancel each other when added.

To remove the correlation between atmospheric and oceanic EAM, we only include the static contribution to ocean bottom pressure into the AAM. Technically, this implies replacing the surface pressure at every grid point over the oceans with the area-mean surface pressure averaged over the whole ocean domain as defined by the AOD1B land-sea mask:

Table 3.1: Long-term mean values of AAM $\chi_{i,p/w}$ calculated over the period 2018 – 2020 that were subtracted from AAM provided by ESMGFZ.

$\chi_{1,p}$	$-1.337335062421382 \cdot 10^{-8}$
$\chi_{2,p}$	$-2.634139096098880 \cdot 10^{-8}$
$\chi_{3,p}$	$+1.990909975815368 \cdot 10^{-10}$
$\chi_{1,w}$	$-3.654088521845072 \cdot 10^{-9}$
$\chi_{2,w}$	$-3.799465410896128 \cdot 10^{-9}$
$\chi_{3,w}$	$+2.812557327707363 \cdot 10^{-8}$

$$p_s(\theta,\phi) = \begin{cases} p_s(\theta,\phi) & \text{at the continents} \\ \dfrac{1}{A_{\text{Oceans}}} \iint\limits_{\text{Oceans}} p_s(\theta,\phi)dA & \text{over the oceans} \end{cases} \tag{3.4}$$

The total mass of the atmosphere is not affected by this operation, but the temporal variability of AAM and its anti-correlation with OAM calculated from an ocean model with atmospheric surface pressure forcing reduces substantially. Note that 13 tidal signals in the atmosphere at S_1, S_2, S_3, and M_2 frequencies and their modulations π_1, P_1, K_1, ψ_1, T_2, R_2, K_2, T_3, R_3 have been estimated and subtracted prior to the replacement of pressure with its area-mean value over the oceans. Further details on the handling of atmospheric tides are provided in Ch. 7.

3.5 Characteristics of AAM From ESMGFZ

AAM from ESMGFZ are integrated every 3 hours from post-processed ECMWF data given at 0.5° equiangular grids. The long-term mean calculated over the period 2018 – 2020 as given in Tab. 3.1 was subtracted from the pressure and wind terms.

AAM mass terms as provided by ESMGFZ note clear seasonalities in all three components, overlaid by weak interannual variations in particular in $\chi_{3,p}$. There are no apparent trends or sudden jumps visible in the data-sets. Compared to the former version GFZ2017, the use of ERA5 atmospheric reanalysis and the updated estimation and removal of tidal signals led only to minor changes in AAM, see Fig. 3.1

The main characteristics of the AAM as described in detail for GFZ2017 in the previous version of this document remain untouched. The axial component $\chi_{3,w}$ of the AAM is characterized by a seasonal signal and substantial interannual variability. Extreme values apparent in the years 1983, 1997, and 2016 are related to strong negative phases of ENSO. There is no apparent trend in the data, and no inconsistencies are identified at the times of transition between ERA5 and the operational ECMWF data.

The residual differences in Fig. 3.2 show a major reduction in erroneous variability with the use of ERA5 instead of ERA40 atmospheric re-analysis until 1979. After 2018 both releases are based on ECMWF operational data with the only difference coming from an updated removal of the tidal signal.

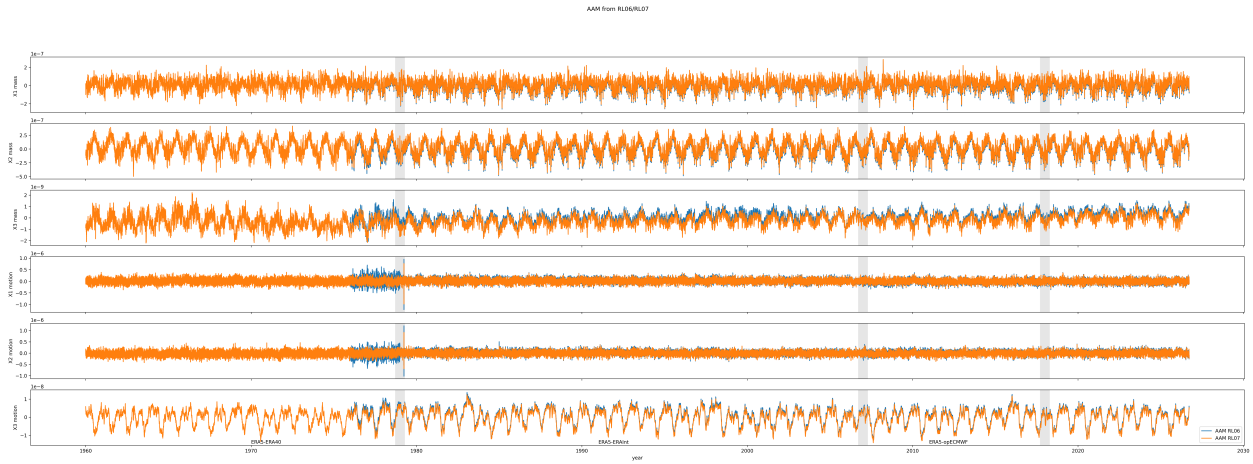


Figure 3.1: AAM mass and motion term time series previous version GFZ2017 and release v2.0.

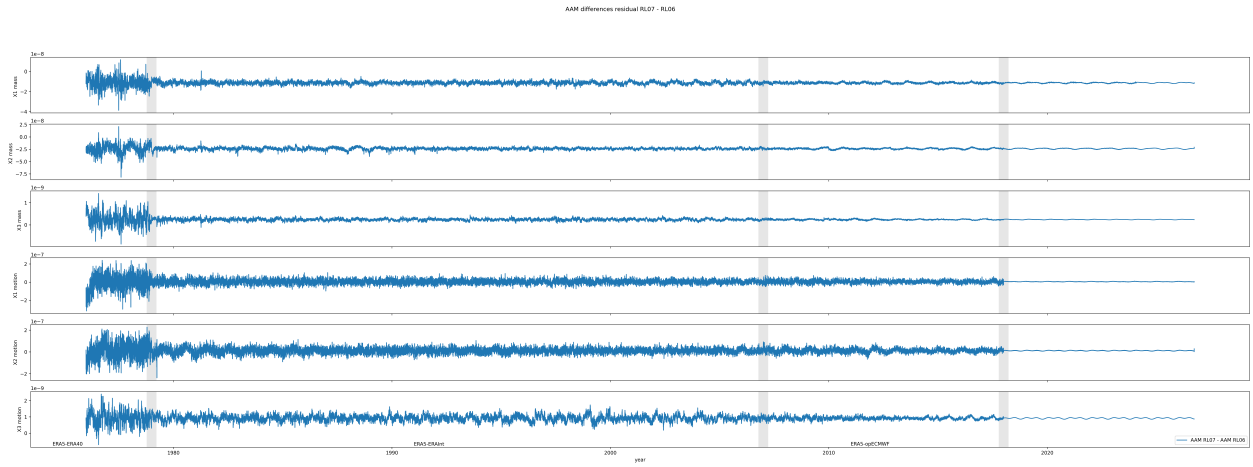


Figure 3.2: Residual differences in AAM mass and motion term time series between previous version GFZ2017 and release v2.0 after removal of the interannual, annual, and semi-annual signal parts.

Chapter 4

Dynamic Ocean EAM From ESMGFZ

Filenames: `ESMGFZ_OAM_v2.0_03h_yyyy.asc`

4.1 OGCM Configuration

Oceanic Effective Angular Momentum functions (OAM) from ESMGFZ are based on a numerical simulation with the Max-Planck-Institute for Meteorology Ocean Model (MPIOM; Jungclaus *et al.*, 2013). It is a general ocean circulation code discretized globally on an Arakawa C-grid in the horizontal, and a z-grid in the vertical. MPIOM includes a sea-ice module (Notz *et al.*, 2013) that utilizes the viscous-plastic rheology of Hibler (1979).

Decades-long numerical model development efforts by Ernst Maier-Reimer (1944 – 2013; Hasselmann, 2013) and his colleagues in Hamburg resulted in a series of high-quality software packages, as, e.g., the Large-Scale Geostrophic Ocean General Circulation Model (LSG; Maier-Reimer & Mikolajewicz, 1992), the Hamburg Ocean Primitive Equation Model HOPE (Drijfhout *et al.*, 1996; Wolff *et al.*, 1997), and the first release of MPIOM (Marsland *et al.*, 2003). The Ocean Model for Circulation and Tides (OMCT; Thomas *et al.*, 2001) used for previous OAM releases is also a direct descendant of HOPE and thus shares many similarities in both physics and numerics with even the current version of MPIOM. The model is forced with atmospheric surface pressure and vertically transfers the momentum to response to surface winds. It contains a dedicated sea-ice module. With the update of MPIOM from AOD1B RL06 to RL 07, the full feedback of self-attraction and loading has been implemented (Shihora *et al.*, 2022b) and the spatial domain has been extended to also include cavities underneath the Antarctic shelf-ice. A medium-resolution configuration of MPIOM is used here that is discretized on a 1.0° tri-polar grid with 40 vertical layers (TP10L40). The internal time-step of the model is 90 min, and ocean state quantities and associated diagnostics as ocean bottom pressure and horizontal currents are stored every 3 hours.

4.2 Atmospheric Forcing Data

Dynamics simulated by MPIOM in our particular model experiment are driven by atmospheric forcing only, and no observational constraints are introduced into the simulation by means of data assimilation. As usual, luni-solar gravitational tides in the oceans are not simulated, but tidal waves in response to periodically varying atmospheric pressure loading and surface winds are part of the simulated ocean bottom pressure field. Those signals are separated during the post-processing from the EAM time-series as discussed in Ch. 7.

The simulation is initialized from 3D temperature and salinity climatologies (Levitus, 2005) followed by a spin-up simulation under cyclic atmospheric forcing conditions with daily sampling as prepared for an ocean model intercomparison project (Röske, 2005). The spin-up simulation has been integrated over 499 years, remaining trends in ocean bottom pressure are less than ± 3 Pa a^{-1} on regional scales, and ± 12 Pa a^{-1} even for individual grid points. The spin-up is followed by a transient simulation with 3 hourly atmospheric forcing obtained from ERA5 for the period 1960 – 2017, and from the operational ECMWF data for all subsequent years.

MPIOM requires the following atmospheric forcing data-sets: atmospheric surface pressure; horizontal surface wind stress, surface wind speed, temperature as well as dew point temperature at 2 m above the surface; cloud cover, short-wave incoming radiation at the surface, and precipitation. Wind stress is derived from horizontal winds at 10 m above ground, density of air at the lowest model level as defined by temperature and specific humidity, and the Charnock parameter that characterizes the roughness of the sea-surface (Beljaars, 1997). The instantaneous horizontal wind stress components are calculated by employing FORTRAN routines provided by ECMWF that are consistent with the IFS cycle 23r1 (Anton Beljaars, pers. communication, 2004).

4.3 Post-Processing of Simulated Bottom Pressure

Ocean bottom pressure is a standard output variable of MPIOM that hydrostatically sums the contributions of air and water pressure along the plumb line. In order to separate the oceanic contribution to ocean bottom pressure, the atmospheric surface pressure applied as a forcing data-set is subtracted. Subsequently, tidal fluctuations as discussed in Ch. 7 are estimated and removed, and the long-term mean ocean bottom pressure averaged over the period 2018 – 2020 is subtracted to arrive at pressure anomalies. Further, pressure anomalies are inverse-barometrically corrected by re-adding the difference between the local pressure and the mean pressure averaged over the whole ocean domain. In order to finally remove any fluctuations in total ocean mass induced by the Boussinesq approximation employed in the ocean model momentum equations as discussed by Greatbatch (1994), the mean bottom pressure averaged over the whole ocean domain is removed by subtracting a homogeneous shell of mass at every time-step:

$$p_b'(\theta,\phi) = p_b(\theta,\phi) - \frac{1}{A_{\text{Oceans}}} \iint\limits_{\text{Oceans}} p_b(\theta,\phi) dA \tag{4.1}$$

4.4 Post-Processing of Simulated Mass Transport Streamfunction

The ocean mass transport streamfunction is a standard output variable of MPIOM that summarizes the barotropic mass transport. From the streamfunction ψ_{tp} we derive the mass transport Tu_{tp} in eastward and Tv_{tp} in southward direction by

$$Tu_{tp} = \frac{d\psi_{tp}}{dSouth} \qquad Tv_{tp} = \frac{d\psi_{tp}}{dEast} \tag{4.2}$$

with $dSouth$ and $dEast$ as local gridspacing in rotated latitude and longitude direction of the tripolar TP10 grid.

Prior to the calculation of the streamfunction derivatives, the undefined land gridcells along the coastline are filled with values of its nearest neighbours. The derivatives are calculated directly in the tripolar TP10 MPIOM grid. As the Arctic seamline between the two Northern poles introduces a sign switch in the u component, we have to smooth the most northern gridcells before unrotating

Table 4.1: Long-term mean values of OAM $\chi_{i,p/w}$ calculated over the period 2018 – 2020 that were subtracted from OAM data provided by ESMGFZ.

$\chi_{1,p}$	$+1.261531253854100 \cdot 10^{-8}$
$\chi_{2,p}$	$+1.348327565073154 \cdot 10^{-8}$
$\chi_{3,p}$	$-2.260473920409492 \cdot 10^{-11}$
$\chi_{1,w}$	$-4.718753433990881 \cdot 10^{-8}$
$\chi_{2,w}$	$+7.560811315928890 \cdot 10^{-8}$
$\chi_{3,w}$	$+3.387603116053778 \cdot 10^{-9}$

Tu_{tp} and Tv_{tp} to geopgraphical East/North components Tu_{geo} and Tv_{geo}. For the bilinear vector interpolation to an regular 0.5° equiangular grid we transform the geographical East/North components Tu_{geo} and Tv_{geo} to intermediate Cartesian 3D vectors and project them back to true East and North directions as Tu_{reg} and Tv_{reg}.

In contrast to derive the mass transports directly on the tripolar TP10 MPIOM grid, the former version of OAM GFZ2017 used a bilinear interpolation of the tripolar streamfunction to a regular 0.5° grid prior to perform the calculation of the derivatives. Thereby erroneous artifact were mapped from the discontinuity along the Antarctic seamline down into mid-latitudes.

Subsequently, tidal fluctuations as discussed in Ch. 7 are estimated and removed, and the long-term means averaged over the period 2018 – 2020 are subtracted to arrive at mass transport anomalies. Finally, to calculate the OAM motion term according to Eq. 2.2, we introduce the mass transport as product of velocity and mass,

$$Tu_{reg} = U \cdot m(\Theta, \Phi) \qquad Tv_{reg} = V \cdot m(\Theta, \Phi) \tag{4.3}$$

4.5 Characteristics of OAM From ESMGFZ

OAM from ESMGFZ are integrated every 3 hours from post-processed MPIOM ocean model data given at the original 1.0° tri-polar TP10 grids remapped to 0.5° regular grids. The long-term mean calculated over the period 2018 – 2020 as given in Tab. 4.1 was subtracted from the ocean pressure and current terms.

In the OAM mass and motion terms as provided by ESMGFZ we note clear seasonalities in particular in the third component, overlaid by weak interannual variations. There are no apparent trends or sudden jumps visible in the data-sets. Compared to the former version GFZ2017, the use of ERA5 atmospheric reanalysis and the updated estimation and removal of tidal signals led only to minor changes in OAM, see Fig. 4.1

The updated retrieval of ocean mass transports for the calculation of the OAM motion terms led to the slightly reduced seasonal amplitudes when compared to OAM motion terms from GFZ2017 (ESMGFZ v1.0).

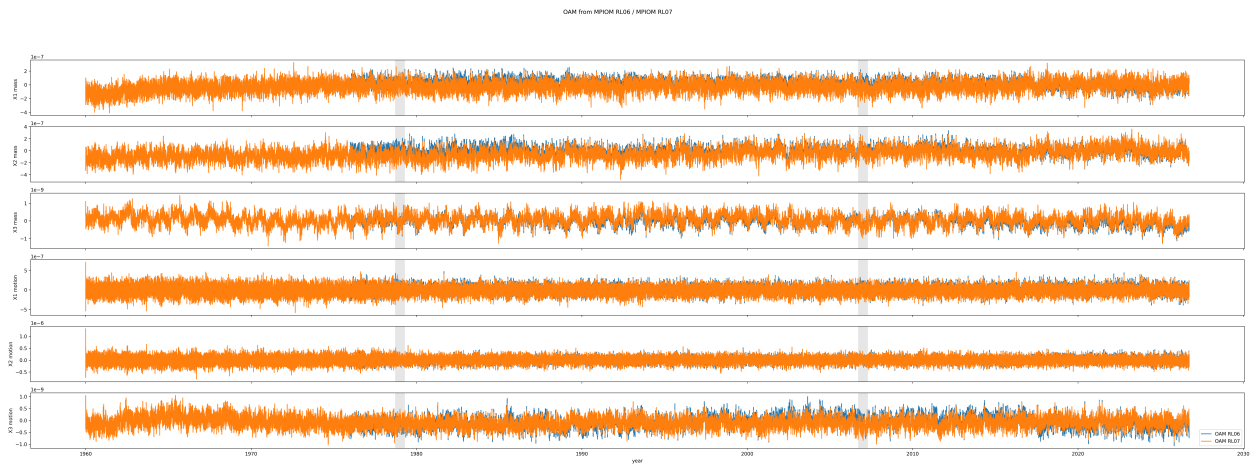


Figure 4.1: OAM mass and motion term time series from previous version GFZ2017 and release v2.0.

Chapter 5

Terrestrial Hydrosphere EAM From ESMGFZ

Filenames: `ESMGFZ_HAM_v2.0_24h_yyyy.asc`

5.1 LISFLOOD Model Experiment

Hydrospheric Effective Angular Momentum functions (HAM) are calculated from terrestrial water storage and flows simulated with the hydrological model OS LISFLOOD (De Roo *et al.*, 2026). OS LISFLOOD provides an independent representation of terrestrial hydrology, including interception, snow accumulation and melt, evapotranspiration, infiltration, soil-water redistribution (represented using three soil layers), preferential flow, groundwater storage and baseflow, surface runoff, and river routing. With a spatial sampling of up to about 5km (0.05°) LISFLOOD can resolves even small surface water compartments like narrow rivers and small lakes. We use the latest release v5.0.0 that includes a routine developed at GFZ (Jensen *et al.*, 2025) to generate vertically integrated terrestrial water storage (TWS) distributed over surface water bodies like lakes and reservoirs as output variable. HAM mass terms are derived from TWS. The horizontal water transport – realized as momentum from velocity and mass – leads to the HAM motion terms.

5.2 Atmospheric Forcing Data

LISFLOOD is driven by daily 2m-temperatures, precipitation, and evaporation from ECMWF ERA5 for the years 1960 – 2017 and from the operational ECMWF data for all later years. Note that all temperature forcing fields from 2018 on are corrected for orographic effects by utilizing a common reference orography as described in Sect. 3.2. The atmospheric forcing for OS LISFLOOD is consistent to the atmospheric data used for the calculation of AAM and also to GFZ's AOD1B RL07 products.

5.3 Characteristics of HAM From ESMGFZ

HAM from ESMGFZ are integrated every day from the post-processed LISFLOOD model data discretized at 0.05° regular grids. For HAM mass terms a long-term mean calculated over the period 2018 – 2020 as given in Tab. 5.1 was subtracted.

Table 5.1: Long-term mean values of HAM water storage terms χ_i calculated over the period 2018 – 2020 that were subtracted from HAM data provided by ESMGFZ.

χ_1	$-8.48246 \cdot 10^{-6}$
χ_2	$-7.67720 \cdot 10^{-6}$
χ_3	$+1.97321 \cdot 10^{-7}$

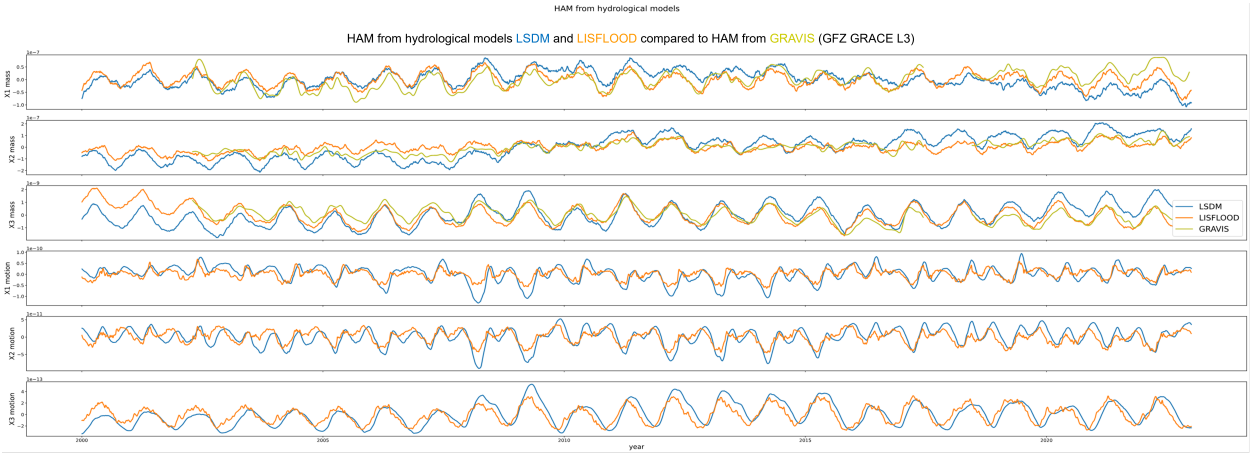


Figure 5.1: HAM mass term time series from previous version GFZ2017 based on LSDM, release v2.0 based on LISFLOOD, and GRAVIS L3 products based on GRACE satellite observation.

HAM motion terms are three orders of magnitude smaller than the HAM mass terms and are therefore often neglected in Earth rotation excitation analyses.

OS LISFLOOD forced with ERA5 shows much more long-term stable HAM when compared to GFZ2017 HAM based on the hydrological model LSDM forced with ERA40 and ERA-Interim, see Fig. 5.1 for the full time series and Fig. 5.2 for the interannual variations only.

Long-term (decadal) trends are not captured in model-based HAM, presumbably due to the melting of ice in Greenland and Antarctica captured by the GRACE mission but not included in the LSDM or LISFLOOD simulation. Low-frequency variability apart from trends, however, is simulated quite well by the numerical model.

The seasonal cycle in χ_1 and χ_2 shows an improved agreement in phase compared to the GRACE based GRAVIS estimates, see Fig. 5.3.

In detail the annual and semi-annual amplitude and phase for the LISFLOOD-ERA5-based HAM mass terms agrees significantly better to GRACE-based estimates and GAO calculated from EOP observational time series than the LSDM based HAM, see Fig. 5.4.

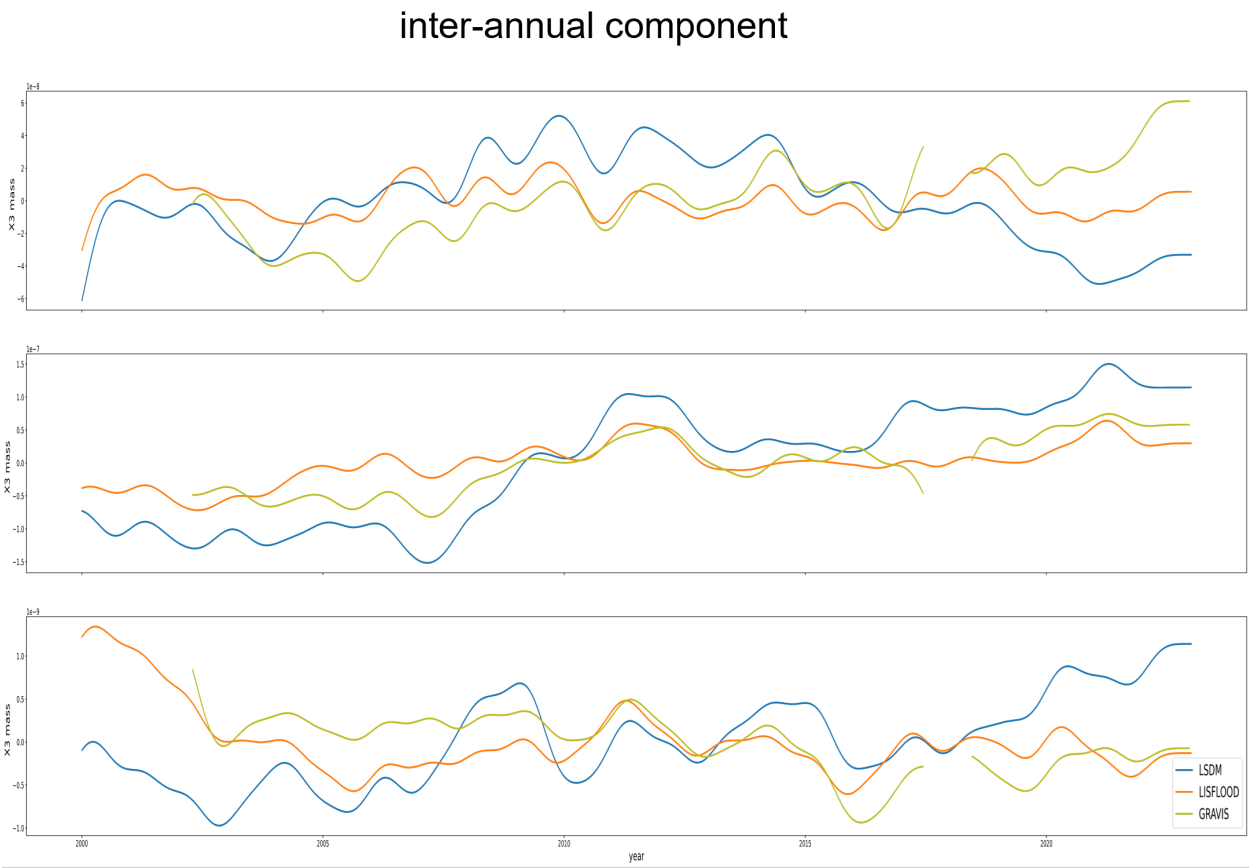


Figure 5.2: Interannual signal in HAM mass term time series from previous version GFZ2017 based on LSDM, release v2.0 based on LISFLOOD, and GRAVIS L3 products based on GRACE satellite observation.

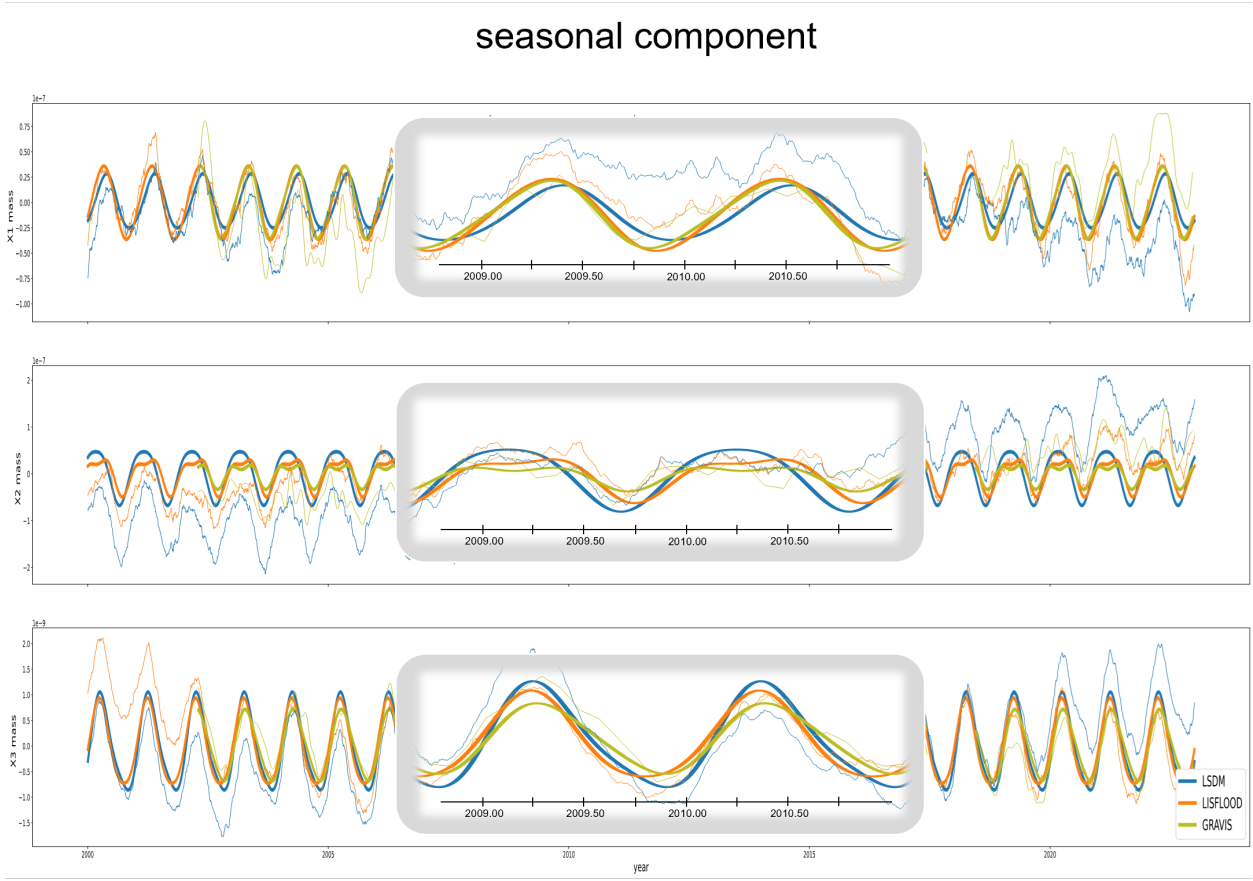
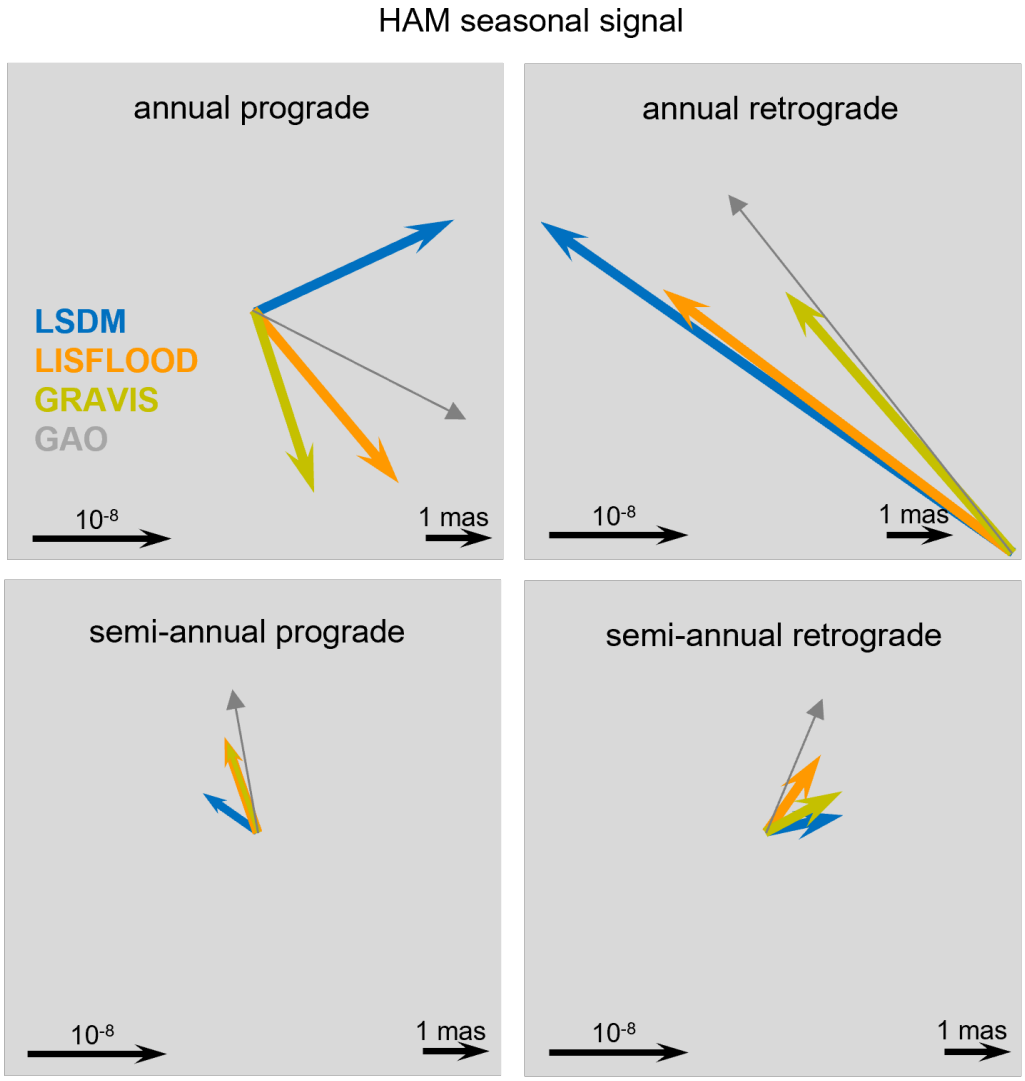


Figure 5.3: Seasonal signal in HAM mass term time series from previous version GFZ2017 based on LSDM, release v2.0 based on LISFLOOD, and GRAVIS L3 products based on GRACE satellite observation.



LSDM: HAM RL06 based on TWS from LSDM
LISFLOOD: HAM RL07 based on TWS simulated by OS LISFLOOD
GRAVIS: HAM based on TWS from GFZ's GRACE/-FO L3 product
GAO = GAM – AAM – OAM from: Nastula, J., Śliwińska, J., Kur, T. et al.
Preliminary study on hydrological angular momentum determined from
CMIP6 historical simulations.
Earth Planets Space 74, 84 (2022). https://doi.org/10.1186/s40623-022-01636-z

Figure 5.4: Annual and semi-annual signal in HAM mass term time series from previous version GFZ2017 based on LSDM, release v2.0 based on LISFLOOD, and GRAVIS L3 products based on GRACE satellite observation compared to the residual GAO signal from EOP observation.

Chapter 6

Barystatic Sea-Level Equation EAM From ESMGFZ

Filenames: `ESMGFZ_SLAM_v2.0_24h_yyyy.asc`

6.1 Global Mass Conservation Approach

Matter at the Earth surface in general and water masses in particular are continuously re-distributed between atmosphere, oceans, and various terrestrial storages including ice-sheets, surface water bodies, soil moisture, and groundwater aquifers. The global water budget is typically not closed in numerical model data-sets. It is in particular not closed in the data-sets underlying the EAM from ESMGFZ, since atmospheric fluxes as precipitation and evaporation are not part of the atmospheric analyses calculated at ECMWF, but instead are taken from high-resolution deterministic forecast model runs initialized from the analyses only.

The consideration of the global mass balance effects is, however, particularly important for seasonal variations in the Length-of-Day (Yan & Chao, 2012). We therefore assume that the total mass in atmosphere, oceans, and all land storages should be constant at any given time. Eventually missing mass is further assumed to be stored in the oceans only.

Any net-inflow of water masses into the oceans will cause a barystatic increase in ocean mass. The actual geographic position of that inflow is not important, since pressure gradients imposed at the surface of the ocean by an inflow of water will trigger barotropic gravity waves that effectively adjust the global sea-level almost instantaneously. Thus, sea-level primarily depends on the accumulated global water fluxes only.

6.2 Sea-Level Variations Inferred From LISFLOOD and ECMWF

To approximate barystatic sea-level variations and to account for the global mass balance among AAM, OAM and HAM, we integrate all atmospheric and terrestrial masses as represented by LISFLOOD and ECMWF over the whole globe at any time-step. Note that global masses simulated by MPIOM reflecting ocean circulation dynamics are constant as enforced after correcting for effects of the Boussinesq approximation and thus do not need to be considered. The inferred global mean sea-level changes reveal a distinct seasonal variation and also some low-frequency variations from year to year, but only a fairly weak long-term trend.

Additionally, spatially variable relative sea-level pattern due to the effects of self-attraction and loading are calculated. We utilize a simplified algorithm as described by Tamisiea *et al.* (2010) that considers an elastic response of the solid Earth to the imposed surface load; disregards any rotational feedback on the sea-level; and treats lateral ocean boundaries and land surface topography as time-invariant.

6.3 Characteristics of SLAM From ESMGFZ

The spatially variable sea-level variations as inferred from globally integrating masses in LISFLOOD and ECMWF under consideration of self-attraction and loading are utilized to calculate barystatic sea-level EAM functions (SLAM). All three components are dominated by the global homogeneous barystatic sea-level anomaly and are thus strongly correlated.

6.4 Comparison With GRACE-Based SLAM From GFZ

We utilize barystatic sea-level estimates from GRACE satellite gravimetry calculated from RL07 spherical harmonic solutions of GFZ (Dahle *et al.*, 2018) derived by following Bergmann-Wolf *et al.* (2014) with the additional consideration of spatially variable self attraction and loading pattern (Tamisiea *et al.*, 2010). The data is publicly available from the new GRAVIS portal accessible at `gravis.gfz-potsdam.de`. Whereas the seasonal cycle is captured rather well in any of the components, we note a strong underestimation of the secular trend in barystatic sea-level from the numerical model, which consequently translates in strongly underestimated linear trends in all three components of SLAM. The direct comparison of SLAM from GRACE and ESMGFZ fully confirms those findings...
ADD LATEST RESULTS FROM ABOUT SLAM COMPARISONS HERE

Chapter 7

Tidal Signals in EAM From ESMGFZ

7.1 Fundamentals on Atmospheric Tides

Atmospheric tides are to be understood here as periodic variations of atmospheric pressure relative to the moving surface of the Earth, which is the Earth's crustal surface in continental regions, and the ocean surface elsewhere. These tides are conventionally observed by pressure gauges attached to the ground, or tied to floating objects as buoys or ships.

Tides in the atmosphere are excited by two different mechanisms that are principally known already for decades: First, absorption of solar radiation by both water vapor and ozone creates large periodic temperature variations in the middle atmosphere that propagate vertically as approximately described by the thermal wind equations and cause large-scale variations in atmospheric surface pressure. The frequencies of this process are fundamentally governed by the incidence angle of solar radiation, so that periods of 24 hours and overtones may occur. The signals are not strictly periodic but vary in amplitude due to seasonal changes in solar insolation, changes in the atmospheric density of the lower troposphere that affects vertical wave propagation, and transient convective processes near the surface that cause periodic pressure variations at periods of 24 hours as well.

Secondly, tides in the atmosphere are excited by direct gravitational attraction of atmospheric masses by the tide-generating bodies sun and moon, and – more importantly – excitation of atmospheric waves by periodic motions of the lower boundary of the atmosphere caused by both tides in the solid Earth and in the oceans. For this process, also secondary gravitational effects due to the modified mass distribution caused by ocean and solid Earth tides add small modifications to the signals.

The representation of surface atmospheric tides in global atmospheric model data has been validated in many aspects with the help of thoroughly screened sets of globally distributed in situ pressure gauges. Those analyses indicate that the principal frequencies S_1 and S_2 are quite well represented by ECMWF, even though a "small but probably significant overestimation of up to 18% for peak semidiurnal amplitudes" is reported (Schindelegger & Ray, 2014).

Signals of the semidiurnal lunar atmospheric tide, which corresponds in frequency to the oceanic tide M_2 have been detected in the 6 hourly fields of the atmospheric re-analysis ERA-Interim by Kohyama & Wallace (2014). Comparison against in situ pressure gauges reveals again a quite good level of agreement (Schindelegger & Dobslaw, 2016). The latter study gives also evidence that the ECMWF assimilation system favorably passes tidal variations measured by in situ pressure and wind data into the global analysis despite of the fact that the physics of in particular the lunar tides are not represented in the ECMWF model. Thus, the appearance of tides in ECMWF is somewhat affected by the evolution of the global observing system, as, for example, demonstrated

Table 7.1: Tidal constituents estimated and removed from AAM and OAM from ESMGFZ.

Doodson Code	Name	Frequency ($°h^{-1}$)	Period (h)
162.556	π_1	14,9178650	24.13214
163.555	P_1	14.9589314	24.06590
164.555	S_1	15.0000000	24.00000
165.555	K_1	15.0410686	23.93000
166.554	ψ_1	15,0821353	23.86930
255.555	M_2	28.9841042	12.42000
272.556	T_2	29.9589333	12.01645
273.555	S_2	30.0000000	12.00000
274.554	R_2	30.0410667	11.98360
275.555	K_2	30.0821373	11.96724
381.555	T_3	44.9589300	8.02738
382.555	S_3	45.0000000	8.00000
383.555	R_3	45.0410700	7.99271

by the disappearance of the M_2 tide after opening of the Panama Canal that redirected commercial shipping routes and thus drastically reduced the number of observations in other parts of the world (see Schindelegger & Dobslaw, 2016, Sect. 5).

Despite of the overall good agreement between ECMWF and in situ pressure gauges, some discrepancies have been identified for M_2 in oceanic regions with strong ocean tides that move atmospheric pressure sensors attached to buoys or ships periodically to different geopotential heights: prominent examples are the signals in the Gulf of Alaska and around the British Isles. Those signals are neither present in free simulations of the lunar tide nor in global fields derived from properly corrected in situ observations (Schindelegger & Dobslaw, 2016).

To some extent, changes in the atmospheric tides on interannual to decadal scales have been also studied for both S_1 (Schindelegger *et al.*, 2016) and S_2 (Diaz-Argandona *et al.*, 2016). Changes from year to year are present in all global atmospheric reanalysis data sets considered, but they deviate strongly when compared to each other. Further research should be devoted to the assessment of interannual variations of atmospheric tides in particular also in the context of long-term changes in atmospheric composition and temperature, but in view of the demonstrated sensitivity of the ECMWF assimilation system to changes in the observing system, it is likely that all the tidal variations seen in the current global atmospheric data-sets still contain systematic errors; see, e.g., Sterl (2004) for a detailed discussion of the consequences of low observation density at middle-to-polar latitudes in global atmospheric reanalyses. Moreover, spurious tidal structures may emerge when predefined assimilation techniques respond to abrupt changes in the types and volumes of observations. Robertson *et al.* (2011) provide evidence that the introduction of new satellite data typically results in perturbations of energy fluxes and modelled moisture, which are important variables in the generation of the diurnal atmospheric tide. In-situ data might be considered as the more reliable and robust source for tidal signals, yet the sampling over several critical areas (equatorial oceans, Amazon, Central Africa) is quite sparse to accurately constrain atmospheric models by an observed tide.

Based on a thorough pre-assessment of the tidal signals in the ECMWF data-set to be used for AAM calculation, we selected the following strategy to cope with atmospheric tides:

- In total 13 tidal frequencies are estimated and removed from the ECMWF surface pressure and wind fields. This includes the main solar tides S_1, S_2, and S_3 as well as the main semidiurnal lunar tide M_2. For each of the four central frequencies additional side-bands are estimated in order to also account for potential modulations (Tab. 7.1) during the year.
- Tidal signals are estimated for the periods 2018 – 2020 for EAM from 2018 and later.
- Before 2018, we use ERA5 reanalysis data, therefore tidal signals are estimated for the periods 2007 – 2014 for EAM periods 2007 – 2017.
- Since interannual variations in atmospheric tides have been found to be less reliable in older years, tidal signals at the 13 selected frequencies have been estimated and removed for each year separately before 2007.

In total, 13 frequencies are considered to be relevant for the removal of atmospheric tides. Here, we employ standard oceanographic naming conventions introduced by Arthur Thomas Doodson, which consequently implies to label the main semi-diurnal lunar tide as M_2. Note that in the meteorologic or aeronomic literature, this frequency is often labelled as L_2. For the naming conventions of S_3 modulations, we follow the suggestions by Ray & Poulouse (2005), phase conventions applied for S_1 are consistent with Ray & Egbert (2004). The tidal arguments applied are given in Tab. 7.1.

7.2 Oceanic Response to Atmospheric Tides

Periodic changes in atmospheric surface pressure over the oceans pose a time-variable loading to the water column that is not fully compensated isostatically, but excite a periodic motion in the oceans itself that adds to the field of lunisolar gravitational ocean tides. The MPIOM simulation used for OAM calculation is forced with atmospheric conditions including atmospheric surface pressure obtained from ECMWF. By doing so, the oceanic response to atmospheric tides is simulated together with the transient non-tidal ocean circulation variability. However, the quality of the simulated tidal fields is affected by a number of limitations in the modeling approach as outlined below:

(i) The atmospheric forcing is applied only every 3 hours and interpolated linearly to the internal model time-step so that atmospheric pressure and wind variability at tidal frequencies is somewhat underestimated in many areas depending on the actual phase of the tidal wave in relation to the time-stepping of the atmospheric forcing. (ii) The spatial resolution of MPIOM is only 1° on average, which is very coarse compared to current state-of-the-art tidal simulations. In particular the dynamics in semi-enclosed seas are often only poorly represented in such a setting. (iii) Currently available model data-sets of the global ocean tides are either based on a combination of observations from satellite altimetry and other sources (GOT4.7, EOT11a); or hydrodynamic simulations that assimilate altimetry, gravimetry, or even tide gauge data (FES2014). MPIOM simulations, instead, do not assimilate any data but are governed by the applied atmospheric forcing only. In view of those limitations, we remove the tidal variability at 13 selected frequencies from the OAM in the same way as from the AAM.

Chapter 8

Earth Orientation Prediction With EAM Forecasts

Filenames: `ESMGFZ_AAM_v2.0_03h_yyyy_dddF.asc`
`ESMGFZ_OAM_v2.0_03h_yyyy_dddF.asc`
`ESMGFZ_HAM_v2.0_24h_yyyy_dddF.asc`
`ESMGFZ_SLAM_v2.0_24h_yyyy_dddF.asc`

8.1 Earth Orientation Prediction Approaches

The availability of Earth orientation parameters (EOP) from space geodetic observations is always delayed by a certain time period due to the need of collecting observations from different sources, runtime of the processing software; necessary quality and plausibility checks; and finally the dissemination to the users. For operational applications in, e.g., satellite navigation, terrestrial astronomy, and satellite-based Earth observations, predictions of EOP for up to 90 days into the future are required.

Various different EOP prediction approaches have been tested within an operational setting during the Earth Orientation Parameters Prediction Comparison Campaign (EOP PCC) running from 2005 until 2008 (Kalarus *et al.*, 2010). During that campaign, valid predictions were required to be submitted once every week. The quality of those predictions was only evaluated later when a finally processed EOP C04 series (Bizouard & Gambis, 2009) based on observations became available.

A substantial portion of the EOP variability can be predicted by classical least-squares extrapolation (LS). Signals at discrete frequencies found to be largely deterministic are estimated over a number of years from C04. Amplitudes and phases obtained are subsequently used for extrapolation into the future. Periods typically considered include the Chandler period as well as the annual and semi-annual harmonics (Kosek, 2012).

To describe the high-frequency variability in EOP induced by non-tidal atmosphere and ocean dynamics, auto-regressive (AR) modeling approaches are applied (Kosek, 2002). Such models are often tuned to realistically reproduce oscillations with periods shorter than 90 days or so. AR modeling is typically combined with LS, and various extensions to the concept have been proposed in the more recent past including the consideration of more than one AR prediction step or multivariate autoregressive prediction (Niedzielski & Kosek, 2012).

Information about high-frequency variability might be also obtained from forecasted EAM functions of the surface geophysical fluids. AAM forecasts contribute to the prediction of ΔUT1 for some

time already (Freedman *et al.*, 1994; Gross *et al.*, 1998; Gambis *et al.*, 2011), which is largely due to the dominance of zonal tropospheric winds for LOD. For polar motion prediction, solely forecasted AAM do not yield notable improvements, since contributions from ocean dynamics and terrestrial water storage are also relevant (Dill & Dobslaw, 2010; Dill *et al.*, 2013). Since many years GFZ provides a complete set of EAM forecasts (AAM, OAM, HAM, SLAM). Their forecast horizon was recently extended from 6 days to 10 days, although atmospheric forecasts appeared to have substantial prediction skills up to day 5 only. OAM and HAM were found to contain some useful information on longer prediction horizons indicating that low-frequency oceanic and hydrospheric processes can substantially extend the window of predictability (Dill & Dobslaw, 2013). In order to exploit EAM data for longer ERP prediction horizons, GFZ developed the EAM Predictor (Dobslaw & Dill, 2018; Dill *et al.*, 2019) which yields combined EAM predictions up to 90 day into the future. From those EAM predictions, ERP can be readily obtained via the Liouville equation by introducing observed ERP from any rapid processing chain of multi-technique geodetic data (e.g., the IERS file finals.daily) as initial values. When reviewing the currently available OAM, HAM and SLAM forecasts issued by GFZ, a continuously growing forecast error with increasing forecast horizons is apparent. Accordingly, their excellent prediction efficiacy in the first days gradually reduces with increasing leadtime. In contrast, the equatorial AAM motion term forecasts show much lower prediction skills, especially for the first 3 days. To mitigate those deficits, the sub-daily variability can be reduced by smoothing the AAM data, albeit on the expense of losing temporal detail. By using a convolutional neural network, a prediction algorithm can be specifically trained to ignore such systematic AAM forecast errors while extracting only the reliable information (Dill *et al.*, 2021). Although the systematic errors in the other EAM forecast components are much lower, such a machine learning-based error correction technique can be beneficial as well (Modiri *et al.*, 2020).

To increase international collaboration and foster further innovation in ERP prediction, IERS established in the year 2021 the 2nd Earth Orientation Prediction Comparison Campaign (2nd EOPPCC; `http://eoppcc.cbk.waw.pl/`). Final results of the campaign revealed that any prediction algorithm outperforming the official IERS prediction announced in Bulletin A indeed used EAM forecasts, at least those from the atmosphere (Kur *et al.*, 2022, 2024; Sliwinska-Bronowicz *et al.*, 2024). Prediction techniques categorized as LS+AR+EAM show a noticeable increase in the mean absolute error (MAE) after a few forecast days that correlates well with the end of the 6-day EAM forecasts. Best prediction methods as identified by the 2nd EOPPCC implicitly mitigate EAM forecast errors by a combination of EAM forecasts with EAM analysis data (Dill *et al.*, 2019).

8.2 AAM, OAM, HAM, and SLAM Forecasts for 10 Days

EAM forecasts are calculated from ECMWF atmospheric forecast data and associated MPIOM and LISFLOOD model forecast runs. As for the analysis runs, atmospheric and oceanic tides were removed from the model forecast states by harmonic analysis of 13 major tidal constituents (S1, S2, S3, and M2 frequencies and their modulations), separately for atmospheric wind, atmospheric pressure, ocean bottom pressure, and ocean currents. The model forecast runs are forced with 3-hourly ECMWF atmospheric forecast data for days 1 to 6 into the future. For the days 7 to 10 of each forecast, only 6-hourly sampled ECMWF atmospheric forcing fields are available. The data is linearly resampled to 3h in order to force the ocean model until the end of day 10.

For many of the four different EAM mass terms the prediction skill is well above 0.6 in the first week of forecasting. From day 6 onwards, the skill scores decrease monotonically. This is related to the lower accuracy of atmospheric forecasts longer than 5 days and the necessary linear interpolation of

the 6-hourly atmospheric data to force the 3-hourly sampled models after day 6 (Dill *et al.*, 2025). Such effects are not visible in the daily sampled forecasts of HAM and SLAM where the relevant dynamics are dominated by much lower frequencies compared to atmosphere and oceans.

Only few of the EAM motion terms provide valuable predictions for day 7 to 10. The equatorial AAM wind terms feature frequent drops in the skill score during the first three days. The large deviations between the equatorial AAM wind term forecasts and their subsequently available analysis data can be traced back to two different mechanisms. Forecast errors that pop up irregularly in the very-first epochs decrease with prediction length. Here, we found artificial quasi-periodic signals with initial amplitudes larger than the increasing stochastic forecast error. This signal is excited irregularly from day-to-day with arbitrary amplitude and phase and vanishes with increasing forecast length ((Dill *et al.*, 2021). From day 7 onwards, increasing EAM forecast errors are related to the low accuracy of ECMWFs atmospheric forecast data and the reduced 6-hourly sampling instead of the 3-hourly sampling until day 6. Presumably, the reduced sampling of the atmospheric forcing also influences the ocean model state, and consequently the derived OAM (Dill *et al.*, 2025).

8.3 Improved EAM Forecasting with Machine Learning

Filenames: `ESMGFZ_AAM_v2.0_03h_yyyy_dddF10corr.asc`
`ESMGFZ_OAM_v2.0_03h_yyyy_dddF10corr.asc`
`ESMGFZ_AAM_v2.0_Windcorrected_03h_yyyy_dddF.asc`

For the equatorial AAM wind terms $_{1,motion}$, $_{2,motion}$ we have established a successfully trained convolutional neural network (CNN) for day 1 to 6 (Dill *et al.*, 2021), see Fig. 8.1. For day 5 to 10 we set up a simpler feedforward neural network (FNN) with less parameters to be trained. As both networks are trained on the difference between EAM forecast and EAM analysis, for each EAM contribution individually, we obtain timeseries that can be applied as correction on the original EAM forecast contributions for day 1 – 6 and 5 – 10 (Dill *et al.*, 2025). We applied this correction only on the AAM and OAM mass and motion terms. For continuity also the former AAM forecast with the equatorial wind term only correction (day 1 – 6) is also still provided. HAM and SLAM forecast were not altered.

8.4 90 Days-Long GAM Forecasts for Routine EOP Predictions

Filenames: `ESMGFZ_GAM_IERSC04-90d_03h_yyyy_dddF.asc`

In addition, to the 10-day EAM forecasts, ESMGFZ provides a 90-day GAM forecast product. This product is calculated as a combination of EAM analysis data, geodetic angular momentum (GAM) derived from the official IERS 20C04 EOP time series, rapid EOP time series taken from bulletin A to fill the gap between the last day of 20C04 and today, and 10-day EAM forecasts. The GAM forecast contains EAM data for the last 90-days and a prediction part 90-days into the future with 3-hourly sampling.

The 90 days-long GAM prediction is calculated with the EAM Predictor developed at GFZ (Dobslaw & Dill, 2018; Dill *et al.*, 2019). The EAM Predictor perform two forecast steps: (A) for up to 10 days into the future, where deterministic geophysical forecasts are available and only the residuals between the geodetically observed Earth rotation angular momentum (GAM) and model-based EAM have to be predicted; and (B) for all later days when the full EAM signal – consisting of the sum of model-based EAM and GAM residuals – has to be forecasted. The GAM residuals are

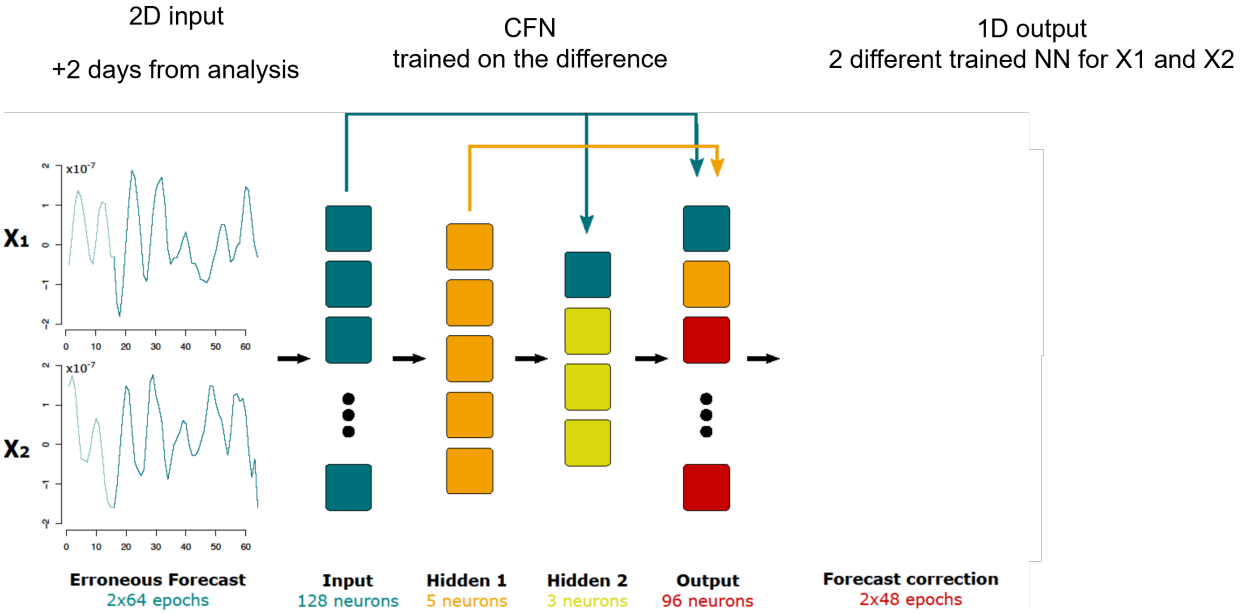


Figure 8.1: Convolutional neural network for the correction of AAM equatorial wind terms (Dill *et al.*, 2021).

extrapolated for the prediction part (A) with daily sampling and subsequently interpolated to 3 hours. The full EAM signal in the prediction part (B) is extrapolated in 3-hourly intervals. For both LS steps we set up the seasonal periods 1, 1/2, and 1/3 years. In addition, we included the 13.66 days period and only for the axial component also 9.13 and 27.4 days, and 3.0 and 9.3 years. Both equatorial components are predicted together as a complex quantity $\chi_1 + i\chi_2$, since those are dynamically coupled as described by the Liouville equation.

For part (A), the sum of all individually modeled final EAM functions from atmosphere, oceans and the terrestrial hydrosphere over the past four years are combined with the latest 10-day forecasts and averaged to arrive at daily values sampled at 12 h UTC. GAM is obtained from C04 augmented by the IERS rapid solutions from bulletin A for the most recent days. For the last four years of data overlap from both series, the residuals between GAM and EAM are calculated. All frequencies indicated above are estimated from this time interval and are subsequently extrapolated forward in time. AR is then applied to the remaining residuals obtained after subtracting the LS fit. For part (B), LS+AR is applied to the full EAM signal obtained from the 3-hourly modeled EAM and the extrapolated GAM residual resampled to 3 h, see Fig. 8.2.

The 90 days-long GAM prediction depends on the reference EOP time series that is predicted. The 90-day-long EAM prediction approach is continuously updated as soon as further improvements are evaluated.

Results from EOP hindcast experiments based on 90 days-long EAM forecasts as calculated over the period 2016 – 2017 are reported in (Dill *et al.*, 2018).

The GAM forecast product as calculated over the period 2020 – 2024 with minor updates in the LS fitting procedure built the basis for the EOP predictions submitted to the 2nd EOP prediction comparison campaign (EOPPCC) as ID 105 and 136. With the latest available EOP coordinates from USNO, made available in bulletin A via CDDIS, as initial value the GAM forecasts were integrated forward in time to obtain a the 90-day EOP predictions for polar motion, UT1-UTC, and dLOD (Kur *et al.*, 2022, 2024; Sliwinska-Bronowicz *et al.*, 2024).

Since 2025, the GAM forecasts are build up on the new IERS 20C04 reference EOP time series.

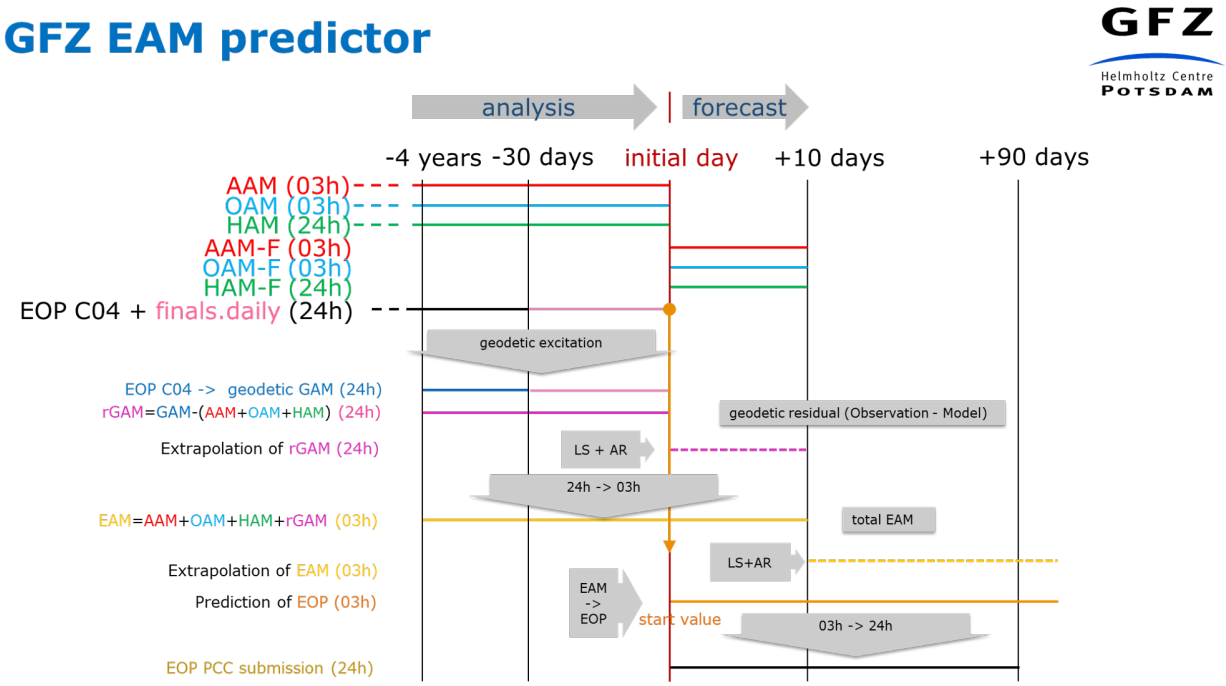


Figure 8.2: ESMGFZ EAM Predictor: EOP prediction on the basis a 2-step GAM forecast that combines GAM from a reference EOP time series with model-based EAM analysis and forecast data.

Furthermore, the extended 10-day EAM forecasts improved by Machine Learning are introduced. These 90 day-long GAM forecasts enter the GFZs EOP predictions submitted as ID 160 to EOP-PCC and 161 to the EOPPCC PML sub-campaign dedicated to Machine Learning based EOP predictions.

References

Adhikari, S. & Ivins, E. R. (2016). Climate-driven polar motion: 2003-2015, *Science Advances*, **2**, e1501,693–e1501,693, DOI:10.1126/sciadv.1501693. 16

Barnes, R. T. H., Hide, R., White, A. A. & Wilson, C. A. (1983). Atmospheric Angular Momentum Fluctuations, Length-of-Day Changes and Polar Motion, *Proceedings of the Royal Society*, **387**, 31–73, DOI:10.1098/rspa.1983.0050. 14

Beljaars, A. C. M. (1997). Air-Sea Interaction in the ECMWF Model, in: *Proc. of Seminar on Atmosphere-Surface Interactions*, ECMWF, Reading, U.K. 26

Bergmann-Wolf, I., Zhang, L. & Dobslaw, H. (2014). Global Eustatic Sea-Level Variations for the Approximation of Geocenter Motion from Grace, *J. Geod. Sci.*, **4**, 37–48, DOI:10.2478/jogs-2014-0006. 16, 36

Bizouard, C. & Gambis, D. (2009). The combined solution C04 for Earth Orientation Parameters consistent with International Terrestrial Reference Frame 2005, *Int. Assoc. Geod. Symp.*, **134**, 265–270. 41

Bizouard, C. & Seoane, L. (2010). Atmospheric and oceanic forcing of the rapid polar motion, *J. Geodesy*, **84**, 19–30, DOI:10.1007/s00190-009-0341-2. 15

Brzeziński, A. (1992). Polar motion excitation by variations of the effective angular momentum function: considerations concerning deconvolution problem, *Manuscripta Geodaetica*, **17**, 3–20. 7, 12

Chao, B. F. & O'Connor, W. P. (1988). Global surface-water-induced seasonal variations in the Earth's rotation and gravitational field, *Geophys. J. Int.*, **94**, 263–270, DOI:10.1111/j.1365-246X.1988.tb05900.x. 16

Chen, J. L. & Wilson, C. R. (2005). Hydrological excitations of polar motion, 1993-2002, *Geophys. J. Int.*, **160**, 833–839, DOI:10.1111/j.1365-246X.2005.02522.x. 16

Cox, G. A., Livermore, P. W. & Mound, J. E. (2016). The observational signature of modelled torsional waves and comparison to geomagnetic jerks, *Physics of the Earth and Planetary Interiors*, **255**, 50–65, DOI:10.1016/j.pepi.2016.03.012. 17

Dahle, C., Flechtner, F., Murböck, M., Michalak, G., Neumayer, K.-H., Abrykosov, O., Reinhold, A. & König, R. (2018). *GRACE geopotential GSM coefficients GFZ RL06*, *Tech. rep.*, GFZ Data Services, DOI:http://doi.org/10.5880/GFZ.GRACE_06_GSM. 36

De Roo, A., Gelati, E., Burek, P., Van der Knijff, J., Wanders, N., Grimaldi, S., Russo, C., Schaffhauser, T., Gomes, G., Nappo, D., Lorini, V., Casado RodrÃguez, J., Carton de Wiart, C., Mazzetti, C., Decremer, D., Mastrantonas, N., Jensen, L., Morrison, O., Moschini, F. & Alfieri, L. (2026). OS LISFLOOD - a distributed hydrological rainfall-runoff model. 7, 29

de Viron, O., Boy, J.-P. & Goosse, H. (2004a). Geodetic effects of the ocean response to atmospheric forcing in an ocean general circulation model, *J. Geophys. Res.*, **109**, B03,411, DOI:10.1029/2003JB002837. 15

de Viron, O., Salstein, D., Bizouard, C. & Fernandez, L. (2004b). Low-frequency excitation of length of day and polar motion by the atmosphere, *J. Geophys. Res.*, **109**, 1–14, DOI:10.1029/2003JB002817. 15

Diaz-Argandona, J., Ezcurra, A., Saenz, J., Ibarra-Berastegi, G. & Errasti, I. (2016). Climatology and temporal evolution of the atmospheric semidiurnal tide in present-day reanalyses, *J. Geophys. Res.*, **121**, 4614–4626, DOI:10.1002/2015JD024513. 38

Dickey, J. O., Marcus, S. L., Johns, C. M., Hide, R. & Thompson, S. R. (1993). The oceanic contribution to the Earth's seasonal angular momentum budget, *Geophys. Res. Lett.*, **20**, 2953–2956, DOI:10.1029/93GL03186. 15

Dill, R. (2008). *Hydrological model LSDM for operational Earth rotation and gravity field variations*, *Tech. rep.*, Scientific Technical Report 08/09, GFZ, Potsdam, DOI:10.2312/GFZ.b103-08095. 8

Dill, R. & Dobslaw, H. (2010). Short-term polar motion forecasts from earth system modeling data, *Journal of Geodesy*, **84**, 529–536. 42

Dill, R. & Dobslaw, H. (2013). Numerical simulations of global-scale high-resolution hydrological crustal deformations, *J. Geophys. Res.*, **118**, 5008–5017, DOI:10.1002/jgrb.50353. 7, 42

Dill, R., Dobslaw, H. & Thomas, M. (2013). Combination of modeled short-term angular momentum function forecasts from atmosphere, ocean, and hydrology with 90-day EOP predictions, *J. Geodesy*, **87**, 567–577, DOI:10.1007/s00190-013-0631-6. 42

Dill, R., Dobslaw, H. & Thomas, M. (2018). Improved 90-day Earth orientation predictions from angular momentum of atmosphere, ocean, and terrestrial hydrosphere, *J. Geodesy*, **92**, DOI:10.1007/s00190-018-1158-7. 44

Dill, R., Dobslaw, H. & Thomas, M. (2019). Improved 90-day earth orientation predictions from angular momentum forecasts of atmosphere, ocean, and terrestrial hydrosphere, *Journal of Geodesy*, **93**, 287–295, DOI:10.1007/s00190-018-1158-7. 42, 43

Dill, R., Saynisch-Wagner, J., Irrgang, C. & Thomas, M. (2021). Improving atmospheric angular momentum forecasts by machine learning, *Earth and Space Science*, **8**, DOI:10.1029/2021EA002070. 42, 43, 44

Dill, R., Stumpe, L., Saynisch-Wagner, J., Thomas, M. & Dobslaw, H. (2025). Benefits of refined 10-day effective angular momentum forecasts for earth rotation parameter prediction, *Journal of Geodesy*, **99**, 1432–1394, DOI:10.1007/s00190-025-01941-x. 9, 43

Dobslaw, H., Bergmann-Wolf, I., Dill, R., Poropat, L., Thomas, M., Dahle, C., Esselborn, S., König, R. & Flechtner, F. (2017). A new high-resolution model of non-tidal atmosphere and ocean mass variability for de-aliasing of satellite gravity observations: AOD1B RL06, *Geophysical Journal International*, **211**, 263–269, DOI:10.1093/gji/ggx302. 7

Dobslaw, H., Bergmann-Wolf, I., Forootan, E., Dahle, C., Mayer-Gürr, T., Kusche, J. & Flechtner, F. (2016). Modeling of present-day atmosphere and ocean non-tidal de-aliasing errors for future gravity mission simulations, *J. Geodesy*, **90**, 1–14, DOI:10.1007/s00190-015-0884-3. 20

Dobslaw, H. & Dill, R. (2018). Predicting Earth orientation changes from global forecasts of atmosphere-hydrosphere dynamics, *Adv. Space Res.*, **61**, 1047–1054, DOI:10.1016/j.asr.2017.11.044. 42, 43

Dobslaw, H., Dill, R., Grötzsch, A., Brzeziński, A. & Thomas, M. (2010). Seasonal polar motion excitation from numerical models of atmosphere, ocean, and continental hydrosphere, *J. Geophys. Res.*, **115**, B10,406, DOI:10.1029/2009JB007127. 8, 16

Dobslaw, H. & Thomas, M. (2005). Atmospheric induced oceanic tides from ECMWF forecasts, *Geophys. Res. Lett.*, **32**, L10,615, DOI:10.1029/2005GL022990. 19

Dobslaw, H. & Thomas, M. (2007). Simulation and observation of global ocean mass anomalies, *J. Geophys. Res.*, **112**, C05,040, DOI:10.1029/2006JC004035. 8

Drijfhout, S., Heinze, C., Latif, M. & Maier-Reimer, E. (1996). Mean Circulation and Internal Variability in an Ocean Primitive Equation Model, DOI:10.1175/1520-0485(1996)026<0559:MCAIVI>2.0.CO;2. 25

Dumberry, M. (2008). Gravitational torque on the inner core and decadal polar motion, *Geophys. J. Int.*, **172**, 903–920, DOI:10.1111/j.1365-246X.2007.03653.x. 16

Eubanks, T. M. (1993). Variations in the orientation of the Earth, in: *Contributions of Space Geodesy to Geodynamics: Earth Dynamics*, vol. 24, p. 1–54, DOI:10.1029/GD024p0001. 14

Freedman, A. P., Steppe, J. A., Dickey, J. O., Eubanks, T. M. & Sung, L. Y. (1994). The Short-Term Prediction of Universal Time and Length-Of-Day Using Atmospheric Angular Momemtum, *J. Geophys. Res.*, **99**, 6981–6996. 42

Gambis, D., Salstein, D. A. & Lambert, S. (2011). Use of atmospheric angular momentum forecasts for UT1 predictions: Analyses over CONT08, *J. Geodesy*, **85**, 435–441, DOI:10.1007/s00190-011-0479-6. 42

Greatbatch, R. J. (1994). A note on the representation of steric sea level in models that conserve volume rather than mass, *J. Geophys. Res.*, **99**, 12,767–12,771, DOI:10.1029/94JC00847. 26

Gross, R. S. (2007). Earth Rotation Variations - Long Period, *Treatise on Geophysics*, **3**, 239–294, DOI:10.1016/B978-044452748-6.00057-2. 11, 13, 14

Gross, R. S. & Chao, B. F. (2006). The rotational and gravitational signature of the December 26, 2004 Sumatran earthquake, *Surv. Geophys.*, **27**, 615–632, DOI:10.1007/s10712-006-9008-1. 17

Gross, R. S., Eubanks, T. M., Steppe, J. A., Freedman, A. P., Dickey, J. O. & Runge, T. F. (1998). A Kalman-filter-based approach to combining independent Earth-orientation series, *J. Geodesy*, **72**, 215–235, DOI:10.1007/s001900050162. 42

Gross, R. S., Fukumori, I. & Menemenlis, D. (2003). Atmospheric and oceanic excitation of the Earth's wobbles during 1980-2000, *J. Geophys. Res.*, **108**, 2370, DOI:10.1029/2002JB002143. 15

Gross, R. S., Fukumori, I. & Menemenlis, D. (2005). Atmospheric and oceanic excitation of decadal-scale Earth orientation variations, *J. Geophys. Res.*, **110**, 1–15, DOI:10.1029/2004JB003565. 15

Gross, R. S., Marcus, S. L., Eubanks, T. M., Dickey, J. O. & Keppenne, C. L. (1996). Detection of an ENSO Signal in Seasonal Length-of-Day Variations, *Geophys. Res. Lett.*, **23**, 3373–3376. 14

Hasselmann, K. (2013). Ernst Maier-Reimer: The discovery of silence, *Nature Geoscience*, **6**, 809–809, DOI:10.1038/ngeo1953. 25

Hense, A., Sündermann, J., Drewes, H., Thomas, M., Chen, X., Dill, R., Müller, M., Seitz, F., Stuck, J., Walter, C. & Winkelnkemper, T. (2009). *Physically consistent system model for the study of the Earth's rotation, surface deformation and gravity field parameters*, *Tech. rep.*, Deutsche Geodätische Kommission, Munich. 8

Hersbach, H., Bell, B., Berrisford, P., Hirahara, S., Horányi, A., Muñoz Sabater, J., Nicolas, J., Peubey, C., Radu, R., Schepers, D., Simmons, A., Soci, C., Abdalla, S., Abellan, X., Balsamo, G., Bechtold, P., Biollo, G., Bidlot, J.-R., Bonavita, M., De Chiara, G., Dahlgren, P., Dee, D., Diamantakis, M., Dragani, R., Flemming, J., Forbes, R., Fuentes, M., Geer, A., Haimberger, L., Healy, S., Hogan, R. J., Hólm, E., Janisková, M., Keeley, S., Laloyaux, P., Lopez, P., Radnoti, G., de Rosnay, P., Rozumenzew, I., Pronk, F., Thépaut, J.-N. & Vitart, F. (2020). The era5 global reanalysis, *Quarterly Journal of the Royal Meteorological Society*, **146**, 1999–2049, DOI:10.1002/qj.3803. 19

Hibler, W. D. (1979). A Dynamic Thermodynamic Sea Ice Model, *J. Phys. Oceanogr.*, **9**, 815–846, DOI:10.1175/1520-0485(1979)009<0815:ADTSIM>2.0.CO;2. 25

Hinderer, J., Legros, H., Jault, D. & Le Mou??l, J. L. (1990). Core-mantle topographic torque: a spherical harmonic approach and implications for the excitation of the Earth's rotation by core motions, *Physics of the Earth and Planetary Interiors*, **59**, 329–341, DOI:10.1016/0031-9201(90)90237-R. 16

Holme, R. (1998). Electromagnetic core-mantle coupling-I. Explaining decadal changes in the length of day, *Geophys. J. Int.*, **132**, 167–180, DOI:10.1046/j.1365-246x.1998.00424.x. 16

Holme, R. & de Viron, O. (2013). Characterization and implications of intradecadal variations in length of day, *Nature*, **499**, 202–204, DOI:10.1038/nature12282. 17

Jensen, L., Dill, R., Balidakis, K., Grimaldi, S., Salamon, P. & Dobslaw, H. (2025). Global 0.05Â° water storage simulations with the osÂ lisflood hydrological model for geodetic applications, *Geophysical Journal International*, **241**, 1840–1852, DOI:10.1093/gji/ggaf129, https://academic.oup.com/gji/article-pdf/241/3/1840/62872588/ggaf129.pdf. 29

Jungclaus, J. H., Fischer, N., Haak, H., Lohmann, K., Marotzke, J., Matei, D., Mikolajewicz, U., Notz, D. & von Storch, J. S. (2013). Characteristics of the ocean simulations in the Max Planck Institute Ocean Model (MPIOM) the ocean component of the MPI-Earth system model, *Journal of Advances in Modeling Earth Systems*, **5**, 422–446, DOI:10.1002/jame.20023. 7, 25

Kalarus, M., Schuh, H., Kosek, W., Akyilmaz, O., Bizouard, C., Gambis, D., Gross, R., Jovanović, B., Kumakshev, S., Kutterer, H., Mendes Cerveira, P. J., Pasynok, S. & Zotov, L. (2010). Achievements of the Earth orientation parameters prediction comparison campaign, *J. Geodesy*, **84**, 587–596, DOI:10.1007/s00190-010-0387-1. 41

Kohyama, T. & Wallace, J. M. (2014). Lunar gravitational atmospheric tide, surface to 50 km in a global, gridded data set, *Geophys. Res. Lett.*, 8660–8665, DOI:10.1002/2014GL060818. 37

Koot, L., de Viron, O. & Dehant, V. (2006). Atmospheric angular momentum Time-series: Characterization of their internal noise and creation of a combined series, *J. Geodesy*, **79**, 663–674, DOI:10.1007/s00190-005-0019-3. 15

Kosek, W. (2002). Autocovariance prediction of complex-valued polar motion time series, *Advances in Space Research*, **30**, 375–380, DOI:10.1016/S0273-1177(02)00310-1. 41

Kosek, W. (2012). Future Improvements in EOP Prediction, *Int. Assoc. Geod. Symp.*, 513–520, DOI:10.1007/978-3-642-20338-1_62. 41

Kur, T., Dobslaw, H., ÅliwiÅska, J., Nastula, J., WiÅska, M. & Partyka, A. (2022). Evaluation of selected short-term predictions of UT1-UTC and LOD collected in the second earth orientation parameters prediction comparison campaign, *Earth, Planets and Space*, **74**, 1880–5981, DOI:https://doi.org/10.1186/s40623-022-01753-9. 42, 44

Kur, T., ÅliwiÅska Bronowicz, J., WiÅska, M., Dobslaw, H., Nastula, J., Partyka, A., Belda, S., Bizouard, C., Boggs, D., Bruni, S., Chen, L., Chin, M., Dhar, S., Dill, R., Duan, P., Ferrandiz, J. M., Gou, J., Gross, R., Guessoum, S., Han, S., Heinkelmann, R., Huang, C., Irrgang, C., Kudrys, J., Li, J., Ligas, M., Liu, L., Lu, W., Mayer, V., Miao, W., Michalczak, M., Modiri, S., Otten, M., Ratcliff, T., Raut, S., Saynisch-Wagner, J., Schartner, M., Schoenemann, E., Schuh, H., Shahvandi, M. K., Soja, B., Su, X., Thaller, D., Thomas, M., Wang, G., Wu, Y., Xu, C., Xu, X., Yang, X., Zhao, X. & Zhou, Z. (2024). Prospects of predicting the polar motion based on the results of the second earth orientation parameters prediction comparison campaign, *Earth and Space Science*, **11**, e2023EA003,278, DOI:https://doi.org/10.1029/2023EA003278, e2023EA003278 2023EA003278, https://agupubs.onlinelibrary.wiley.com/doi/pdf/10.1029/2023EA003278. 42, 44

Levitus, S. (2005). Warming of the world ocean, 1955â2003, *Geophys. Res. Lett.*, **32**, 1–4, DOI:10.1029/2004GL021592. 26

Madzak, M., Schindelegger, M., Böhm, J., Bosch, W. & Hagedoorn, J. (2016). High-frequency Earth rotation variations deduced from altimetry-based ocean tides, *J. Geodesy*, **90**, 1237–1253, DOI:10.1007/s00190-016-0919-4. 17

Maier-Reimer, E. & Mikolajewicz, U. (1992). *The Hamburg Large Scale Geostrophic Ocean General Circulation Model Cycle 1*, *Tech. Rep. 2*, Deutsches Klimarechenzentrum, Hamburg. 25

Marcus, S. L., Chao, Y., Dickey, J. O. & Gegout, P. (1998). Detection and modeling of nontaidal oceanic effects on Earth's rotation rate, *Science*, **281**, 1656–1659. 15

Marshall, J., Adcroft, A., Hill, C., Perelman, L. & Heisey, C. (1997). A finite-volume, incompressible Navier Stokes model for studies of the ocean on parallel computers, *J. Geophys. Res.*, **102**, 5753–5766, DOI:10.1029/96JC02775. 15

Marsland, S. J., Haak, H., Jungclaus, J. H., Latif, M. & Röske, F. (2003). The Max-Planck-Institute global ocean/sea ice model with orthogonal curvilinear coordinates, *Ocean Modelling*, **5**, 91–127, DOI:10.1016/S1463-5003(02)00015-X. 8, 25

Martinec, Z. & Hagedoorn, J. (2014). The rotational feedback on linear-momentum balance in glacial isostatic adjustment, *Geophys. J. Int.*, **199**, 1823–1846, DOI:10.1093/gji/ggu369. 16

Masaki, Y. (2008). Wind field differences between three meteorological reanalysis data sets detected by evaluating atmospheric excitation of Earth rotation, *J. Geophys. Res.*, **113**, DOI:10.1029/2007JD008893. 15

Milne, G. A. & Mitrovica, J. X. (1996). Postglacial sea-level change on a rotating Earth: first results from a gravitationally self-consistent sea-level equation, *Geophys. J. Int.*, **126**, F13–F20, DOI:10.1111/j.1365-246X.1996.tb04691.x. 16

Modiri, S., Belda, S., Hoseini, M., Heinkelmann, R., FerrÃ¡ndiz, J. M. & Schuh, H. (2020). A new hybrid method to improve the ultra-short-term prediction of lod, *Journal of Geodesy*, **94**, 1432–1394, DOI:https://doi.org/10.1007/s00190-020-01354-y. 42

Mound, J. E. & Buffett, B. A. (2003). Interannual oscillations in length of day: Implications for the structure of the mantle and core, *J. Geophys. Res.*, **108**, 17, DOI:2334\rArtn2334. 16

Nam, Y. S. & Dickman, S. R. (1990). Effects of dynamic long-period ocean tides on changes in Earth's rotation rate, *Journal of Geophysical Research*, **95**, 6751, DOI:10.1029/JB095iB05p06751. 14

Nastula, J., Ponte, R. M. & Salstein, D. (2007). Comparison of polar motion excitation series derived from GRACE and from analyses of geophysical fluids, *Geophys. Res. Lett.*, **34**, 2–7, DOI:10.1029/2006GL028983. 16

Nastula, J., Salstein, D. & Kolaczek, B. (2009). Patterns of atmospheric excitation functions of polar motion from high-resolution regional sectors, *J. Geophys. Res.*, **114**, DOI:10.1029/2008JB005605. 15

Neef, L. J. & Matthes, K. (2012). Comparison of Earth rotation excitation in data-constrained and unconstrained atmosphere models, *J. Geophys. Res.*, **117**, D02,107, DOI:10.1029/2011JD016555. 15

Niedzielski, T. & Kosek, W. (2012). Prediction Analysis of UT1-UTC Time Series by Combination of the Least-Squares and Multivariate Autoregressive Method, *Int. Assoc. Geod. Symp.*, 153–157, DOI:10.1007/978-3-642-22078-4_23. 41

Notz, D., Haumann, F. A., Haak, H., Jungclaus, J. H. & Marotzke, J. (2013). Arctic sea-ice evolution as modeled by Max Planck Institute for Meteorology's Earth system model, *Journal of Advances in Modeling Earth Systems*, **5**, 173–194, DOI:10.1002/jame.20016. 25

Petit, G. & Luzum, B. (2010). *IERS Conventions (2010)*, Verlag des Bundesamts für Kartographie und Geodäsie, Frankfurt, 1–179 p. 17

Ponte, R. M. & Rosen, R. D. (1993). Determining torques over the ocean and their role in the planetary momentum budget, *J. Geophys. Res.*, **98**, 7317–7325. 15

Ponte, R. M. & Rosen, R. D. (1994). Oceanic angular momentum and torques in a general circulation model, *J. Phys. Oceanogr.*, **24**, 1966–1977. 15

Ponte, R. M., Stammer, D. & Marshall, J. (1998). Oceanic Signals in observed motions of the Earth's pole of rotation, *Nature*, **391**, 476–479, DOI:10.1038/35126. 15

Ponte, R. M., Stammer, D. & Wunsch, C. (2001). Improving ocean angular momentum estimates using a model constrained by data, *Geophys. Res. Lett.*, **28**, 1775–1778, DOI:10.1029/2000GL011671. 15

Ray, R. D. & Egbert, G. D. (2004). The Global S 1 Tide, *J. Phys. Oceanogr.*, **34**, 1922–1935. 39

Ray, R. D. & Erofeeva, S. Y. (2014). Long-period tidal variations in the length of day, *Journal of Geophysical Research: Solid Earth*, **119**, 1498–1509, DOI:10.1002/2013JB010830. 17

Ray, R. D. & Poulouse, S. (2005). Terdiurnal Surface-Pressure Oscillations over the Continental United States, *Mon. Weather Rev.*, **133**, 2526–2534, DOI:10.1175/MWR2988.1. 39

Rietbroek, R., Brunnabend, S.-E., Kusche, J., Schröter, J. & Dahle, C. (2016). Revisiting the contemporary sea-level budget on global and regional scales, *Proceedings of the National Academy of Sciences*, **113**, 1504–1509, DOI:10.1073/pnas.1519132113. 16

Robertson, F. R., Bosilovich, M. G., Chen, J. & Miller, T. L. (2011). The effect of satellite observing system changes on MERRA water and energy fluxes, *J. Clim.*, **24**, 5197–5217, DOI:10.1175/2011JCLI4227.1. 38

Roeckner, E., Bäuml, G., Bonaventura, L., Brokopf, R., Esch, M., Giorgetta, M., Hagemann, S., Kirchner, I., Kornblueh, L., Rhodin, A., Schlese, U., Schulzweida, U. & Tompkins, A. (2003). The atmospheric general circulation model ECHAM5: Part 1: Model description, *MPI Report*, 1–140, DOI:10.1029/2010JD014036. 8

Röske, F. (2005). Global ocean heat and freshwater forcing datasets based on ERA-40 and ERA-15, in: *Reports on Earth System Science 13*, Max Planck Institute for Meteorology, Hamburg, Germany. 26

Saynisch, J., Wenzel, M. & Schröter, J. (2011). Assimilation of Earth rotation parameters into a global ocean model: length of day excitation, *J. Geodesy*, **85**, 67–73, DOI:10.1007/s00190-010-0416-0. 15

Schindelegger, M. & Dobslaw, H. (2016). A global ground truth view of the lunar air pressure tide L 2, *J. Geophys. Res.*, **121**, 95–110, DOI:10.1002/2015JD024243. 37, 38

Schindelegger, M., Einšpigel, D., Salstein, D. & Böhm, J. (2016). The Global S1 Tide in Earth's Nutation, *Surv. Geophys.*, **37**, 643–680, DOI:10.1007/s10712-016-9365-3. 38

Schindelegger, M. & Ray, R. (2014). Surface Pressure Tide Climatologies Deduced from a Quality-Controlled Network of Barometric Observations, *Mon. Weather Rev.*, **142**, 4872–4889, DOI:10.1175/MWR-D-14-00217.1. 17, 37

Seitz, F. & Schmidt, M. (2005). Atmospheric and oceanic contributions to Chandler wobble excitation determined by wavelet filtering, *J. Geophys. Res.*, **110**, 1–11, DOI:10.1029/2005JB003826. 15

Semtner, A. J. & Chervin, R. M. (1992). Ocean general circulation from a global eddy-resolving model, *J. Geophys. Res.*, **97**, 5493, DOI:10.1029/92JC00095. 15

Seoane, L., Nastula, J., Bizouard, C. & Gambis, D. (2009). The use of gravimetric data from GRACE mission in the understanding of polar motion variations, *Geophys. J. Int.*, **178**, 614–622, DOI:10.1111/j.1365-246X.2009.04181.x. 16

Shihora, L., Balidakis, K., Dill, R., Dahle, C., Ghobadi-Far, K., Bonin, J. & Dobslaw, H. (2022a). Non-tidal background modeling for satellite gravimetry based on operational ecwmf and era5 reanalysis data: Aod1b rl07, *Journal of Geophysical Research: Solid Earth*, **127**, e2022JB024,360, DOI:10.1029/2022JB024360, e2022JB024360 2022JB024360, https://agupubs.onlinelibrary.wiley.com/doi/pdf/10.1029/2022JB024360. 7

Shihora, L., Liu, Z., Balidakis, K., Wilms, J., Dahle, C., Flechtner, F., Dill, R. & Dobslaw, H. (2024). Accounting for residual errors in atmosphereâocean background models applied in satellite gravimetry, *Journal of Geodesy*, **98**, 1432–1394, DOI:10.1007/s00190-024-01832-7. 7

Shihora, L., Sulzbach, R., Dobslaw, H. & Thomas, M. (2022b). Self-attraction and loading feedback on ocean dynamics in both shallow water equations and primitive equations, *Ocean Modelling*, **169**, 101,914, DOI:10.1016/j.ocemod.2021.101914. 25

Sliwinska-Bronowicz, J., Kur, T., WiÅska, M., Dobslaw, H., Nastula, J., Partyka, A., Belda, S., Bizouard, C., Boggs, D., Bruni, S., Chen, L., Chin, M., Dhar, S., Dill, R., Ferrandiz, J. M., Gou, J., Gross, R., Guessoum, S., Han, S., Heinkelmann, R., Irrgang, C., Kiani Shahvandi, M., Li,

J., Ligas, M., Liu, L., Lu, W., Mayer, V., Michalczak, M., Modiri, S., Otten, M., Ratcliff, T., Raut, S., Saynisch-Wagner, J., Schartner, M., Schoenemann, E., Schuh, H., Soja, B., Su, X., Thaller, D., Thomas, M., Wang, G., Wu, Y., Xu, X., Yang, X., Zhao, X. & Zhou, Z. (2024). Assessment of length-of-day and universal time predictions based on the results of the second earth orientation parameters prediction comparison campaign, *Journal of Geodesy*, **98**, 1432–1394, DOI:https://doi.org/10.1007/s00190-024-01824-7. 42, 44

Sterl, A. (2004). On the (in)homogeneity of reanalysis products, *J. Clim.*, **17**, 3866–3873, DOI:10.1175/1520-0442(2004)017<3866:OTIORP>2.0.CO;2. 38

Stuck, J. (2002). *Die simulierte axiale Atmosphärische Drehimpulsbilanz des ECHAM3-T21 GCM*, Ph.D. thesis, University of Bonn. 8

Tamisiea, M. E., Hill, E. M., Ponte, R. M., Davis, J. L., Velicogna, I. & Vinogradova, N. T. (2010). Impact of self-attraction and loading on the annual cycle in sea level, *J. Geophys. Res.*, **115**, C07,004, DOI:10.1029/2009JC005687. 36

Tapley, B. D., Bettadpur, S., Watkins, M. M. & Reigber, C. (2004). The gravity recovery and climate experiment: Mission overview and early results, *Geophys. Res. Lett.*, **31**, 09,607, DOI:10.1029/2004GL019920. 16

Thomas, M., Sündermann, J. & Maier-Reimer, E. (2001). Consideration of ocean tides in an OGCM and impacts on subseasonal to decadal polar motion excitation, *Geophys. Res. Lett.*, **28**, 2457–2460. 8, 15, 25

Walter, C. (2008). *Simulationen hydrologischer Massenvariationen und deren Einfluss auf die Erdrotation*, Ph.D. thesis, Technische Universität Dresden. 8

Wolff, J.-O., Maier-Reimer, E. & Legutke, S. (1997). *The Hamburg Ocean Primitive Equation Model HOPE*, *Tech. Rep. 13*. 25

Wunsch, C. & Stammer, D. (1997). Atmospheric Loading and the Oceanic "Inverted Barometer" Effect, *Rev. Geophys.*, **35**, 79–107, DOI:10.1029/96RG03037. 21

Yan, H. & Chao, B. F. (2012). Effect of global mass conservation among geophysical fluids on the seasonal length of day variation, *J. Geophys. Res.*, **117**, n/a–n/a, DOI:10.1029/2011JB008788. 16, 35

Yessad, K. (2015). *FULL-POS in the Cycle 41T1 of ARPEGE/IFS*, *Tech. rep.*, Meteo-France. 19, 20

Zhong, M. (2003). Atmospheric, hydrological, and ocean current contributions to Earth's annual wobble and length-of-day signals based on output from a climate model, *J. Geophys. Res.*, **108**, 2057, DOI:10.1029/2001JB000457. 15

Zhou, Y. H., Chen, J. L. & Salstein, D. A. (2008). Tropospheric and stratospheric wind contributions to Earth's variable rotation from NCEP/NCAR reanalyses (2000-2005), *Geophys. J. Int.*, **174**, 453–463, DOI:10.1111/j.1365-246X.2008.03843.x. 15

Zhou, Y. H., Salstein, D. A. & Chen, J. L. (2006). Revised atmospheric excitation function series related to Earth's variable rotation under consideration of surface topography, *J. Geophys. Res.*, **111**, DOI:10.1029/2005JD006608. 15

Appendix A

File Format Description

Effective angular momentum function files from ESMGFZ are available for anonymous download via ftp://ig2-dmz.gfz-potsdam.de/EAM. The technical documentation and other release notes are accessible from isdc.gfz-potsdam.de/esmdata/eam.

The data is provided in ascii-files individually for atmosphere dynamics (AAM), ocean circulation effects (OAM), terrestrial water storage variability (HAM), and barystatic sea-level changes (SLAM). Each file contains a header providing information on the processing date, the time-span covered by the data in the file, the long-term mean values that have been subtracted during data processing, and details of the data source and processing details, as, e.g., the reduction of tidal variations.

The header is followed by a data block with one line corresponding to a single time-epoch. Columns 1 to 5 provide the datum information, columns 6 to 8 the mass terms $\chi_{i,p}$, and columns 9 to 11 the motion terms $\chi_{i,w}$ (Tab. A.1). Note that motions terms are only provided for AAM, OAM, HAM and its assciated individual 6 days-long forecasts, but are absent from SLAM and the combined 90 days-long EAM forecasts. All data-sets are organized into yearly files. Files for the current year are replaced on the server as soon as new data becomes available. Forecast files are only available for the most recently issued prediction.

Table A.1: Format details of the data block of the EAM ascii-files provided by ESMGFZ. Motion terms given in columns 9 to 11 are not included in SLAM and 90 days-long EAM forecasts.

Format	Abbreviation	Description
%4s	YYYY	year
%2s	MM	month
%2s	DD	day
%2s	HH	hour in UTC
%9.3f	MJD	Modified Julian Date
%23.15e	x	χ_1 mass term
%23.15e	y	χ_2 mass term
%23.15e	z	χ_3 mass term
%23.15e	x	χ_1 motion term
%23.15e	y	χ_2 motion term
%23.15e	z	χ_3 motion term

Appendix B

Acronyms

AAM	Atmospheric Effective Angular Momentum Functions
AOD1B	GRACE Atmosphere and Ocean De-Aliasing Level-1B Product
AR	Auto-Regressive modelling for ERP prediction
C04	Final EOP C04 series of IERS
CNN	Convolutional neural network
CFN	Convolutional Feedforward network
DWD	Deutscher Wetterdienst - German Meteorological Service
EAM	Effective Angular Momentum Functions
ECHAM5	fifth generation ECMWF / Hamburg atmospheric model
ECMWF	European Centre for Medium-Range Weather Forecasts
ECOCTH	coupled ECHAM5 atmosphere, MPIOM ocean, Tide, and hydrological discharge model
ECCO	Estimating the Circulation and Climate of the Ocean ocean model
ENSO	El NiÃ±o*SouthernOscillation*
EOP	Earth Orientation Parameters
EOP PCC	Earth Orientation Parameters Prediction Comparison Campaign
ERA-40	ECMWF re-analysis of meteorological observations covering 1957 – 2002
ERA-Interim	fourth generation ECMWF atmospheric reanalysis of global climate covering 1979 – 2019
ERA5	fifth generation ECMWF reanalysis for the global climate and weather
ESMDATA	Product repository www.esmdata.gfz.de
ESMGFZ	Earth System Modelling group at GFZ Helmholtz Centre for Geosciences
FNN	Feedforward neural network
GAM	Geodetic Effective Angular Momentum Function
GAO	GAM - AAM - OAM
GFZ	GFZ Helmholtz Centre for Geosciences
GGFC	Global Geophysical Fluids Center
GIA	Glacial Isostatic Adjustment
GRACE	Gravity Recovery And Climate Experiment Satellite Mission
GRACE-FO	GRACE Follow-On mission
GRAVIS	GFZ - Gravity Information Service
HAM	Hydrospheric Effective Angular Momentum Functions
HOPE	Hamburg Ocean Primitive Equation Model
IERS	International Earth Rotation and Reference Systems Service
IFS	Integrated Forecasting System of the ECMWF
JMA	Japanese Meteorological Agency
JPL	Jet Propulsion Laboratory

LOD	length-of-day
LS	Least-Squares modelling for ERP prediction
LSDM	Land Surface and Discharge Model
LSG	Large-Scale Geostrophic Model
MPIOM	Max-Planck-Institute for Meteorology Ocean Model
NCEP	National Centers for Environmental Prediction
NWP	Numerical Weather Prediction
OAM	Oceanic Effective Angular Momentum Functions
OGCM	Ocean General Circulation Model
OMCT	Ocean Model for Circulation and Tides
OS LISFLOOD	Open source hydrological model Lisflood
POCM	Parallel Ocean Circulation Model
RMSD	Root Mean Squared Differences
SLAM	Barystatic Sea-Level Effective Angular Momentum Functions
TUV	Technical University of Vienna
TWS	Terrestrial Water Storage
UT1	Universal Time based on Earth rotation angle
VLBI	Very Long Baseline Interferometry
WMO	World Meteorological Organization